Assessing Non-Ideal Instrumental Effects in High-Resolution FTIR Spectroscopy: Instrument Performance Characterization

Gezahegn Sufa Daba[1,2] and Gizaw Mengistu Tsidu[3]

[1]Department of Physics, Addis Ababa University, P.O. Box 1176, Addis Ababa, Ethiopia
[2]Department of Physics, Debre Birhan University, P.O. Box 405, Debre Birhan, Ethiopia
[3]Department of Earth and Environmental Sciences, Botswana International University of Science and Technology (BIUST), Private Mail Bag 16, Palapye, Botswana

Correspondence: Gezahegn Sufa Daba (gezahegnsufaa@gmail.com)

Abstract. This study investigates the impact of non-ideal instrumental effects on the performance of high-resolution Fourier Transform Infrared (FTIR) spectrometers, with a focus on the Bruker FTS 120M. Key non-idealities, including retroreflector misalignments, baseline drift, and spectral channeling, were systematically analyzed using advanced diagnostic tools such as ALIGN60 and LINEFIT. The nominal configuration exhibited significant anomalies, notably modulation efficiency (ME) deviations of up to +10.9%, phase error (PE) variability of 2.11×10^{-2} radians, and spectral channeling frequencies such as a persistent 2.9044 cm^{-1}, along with emerging frequencies around 0.24 cm^{-1} attributed to retroreflector wear and CaF$_2$ beamsplitter degradation. A pronounced anomaly at 40.672 cm^{-1}, likely induced by environmental factors such as external vibrations or mechanical instability, was also identified. Implementation of a modified configuration successfully mitigated these issues, reducing PE variability to 0.042×10^{-2} radians, aligning ME within the NDACC-acceptable threshold of 1.1, and achieving substantial improvements in the instrument line shape (ILS), including sharper peaks, narrower full-width at half maximum (FWHM), and reduced side-lobe asymmetry. Analysis of HBr transmission spectra revealed improved fitting of the P(6) line, characterized by lower residuals and enhanced spectral quality. Simulated Haidinger fringes near zero path difference (ZPD) highlighted alignment degradation patterns, underscoring the necessity for precise optical adjustments. Temporal trends showed a 14% increase in ILS peak height and significant RMSE reductions in the modified configuration. Overall, this study provides a robust framework for diagnosing and correcting instrumental artifacts, ensuring the accuracy, reproducibility, and long-term stability of FTIR measurements essential for atmospheric trace gas retrievals.

1 Introduction

Fourier Transform Infrared (FTIR) spectroscopy has become a cornerstone technique in atmospheric remote sensing, providing high-resolution, non-invasive measurements of trace gases that are crucial for understanding air quality, climate change, atmospheric composition, and atmospheric dynamics (e.g. Bacsik et al. (2004); Yamanouchi et al. (2021)). Its ability to simultaneously detect and quantify multiple gases with high precision in a single measurement, combined with its robustness and versatility, makes it essential for ground-based monitoring of atmospheric composition and chemistry (Zhou et al., 2022; Zhu et al., 2024). This capability enables FTIR to capture detailed profiles of pollutants like CO, C$_2$H$_6$, HCN, and C$_2$H$_2$, supporting

in-depth analysis of pollutant sources, transport pathways, and transformations in the atmosphere. As a result, FTIR instruments, such as the Bruker IFS 120M, are widely adopted by prominent international networks such as the Network for the Detection of Atmospheric Composition Changes Infrared Working Group (NDACC-IRWG) and the Total Column Observing Network (TCOON) (Wunch et al., 2011; Mazière et al., 2017; Yamanouchi et al., 2023; García et al., 2021). These networks rely on the capabilities of FTIR spectroscopy to deliver consistent, long-term, and high-quality data, which are essential for monitoring changes in atmospheric composition, tracking greenhouse gas trends, and assessing the broader impacts on air quality and climate.

FTIR spectrometry operates by splitting an infrared beam into two paths, one reflecting off a fixed mirror and the other off a moving mirror, before recombining to form an interference pattern that is Fourier-transformed into a spectrum to provide molecular absorption information (Salzer, 2008). Accurate retrievals of atmospheric constituents depend critically on the instrument line shape (ILS), which characterizes the spectral resolution and fidelity (Roche et al., 2021). The ILS impacts spectral accuracy by determining resolution and line shape, with deviations in modulation efficiency (ME) or phase error (PE) leading to discrepancies in spectral fitting (Hase et al., 1999; Hase, 2012; Sun et al., 2018b). Imperfections in the ILS lead to errors in determining total column and partial column amounts of trace gases, ultimately causing potential misinterpretations of atmospheric composition (e.g. Sun et al., 2017; Chesnokova et al., 2019; Langerock et al., 2024). Under nominal conditions, ME approaches unity, and PE remains minimal at zero path difference (ZPD), gradually diminishing with increasing optical path difference (OPD) (Garc'ia et al., 2022). Misalignments such as field stop decentering, retroreflector shear, or scanner bar distortions introduce errors in ME and PE, affecting the measured spectra (e.g. Sun et al., 2017, 2018b). For instance, cosine bending misalignment causes overmodulation, particularly at maximum OPD, which distorts the ILS by artificially broadening or narrowing spectral lines and resulting in inaccuracies in gas concentration retrievals (e.g. Hase, 2012; Sun et al., 2017, 2018b).

Despite the recognized sensitivity of FTIR retrievals to ILS deviations, the NDACC community largely relies on nominal ILS assumptions for trace gas retrievals, often overlooking the impact of misalignments and spectroscopic artifacts on spectral accuracy (e.g. Liu et al., 2021b; García et al., 2021; Smale et al., 2023). Although theoretical studies have investigated the effects of instrumental misalignments on column retrievals of NDACC standard gases through simulations, empirical validation using real-world instrumental setups remains limited (e.g. Sun et al., 2018b). Additionally, spectroscopic artifacts such as baseline drift, spectral channeling, and DC offsets , which are common in field operations, are frequently underreported or uncorrected in routine analyses (e.g. Abrams et al., 1994; Salomaa and Kauppinen, 1998; Blumenstock et al., 2021; Yamanouchi et al., 2023). The absence of standardized protocols for identifying and correcting these artifacts introduces systematic biases into long-term data records, undermining the reliability and reproducibility of FTIR-based atmospheric measurements. These gaps in addressing practical ILS imperfections and spectroscopic artifacts highlight a critical research need: to move beyond theoretical simulations toward real-world diagnostics and corrections. Without systematic evaluation and mitigation of instrumental non-idealities, the precision and comparability of trace gas retrievals across global networks remain compromised, limiting the broader utility of FTIR observations for atmospheric science.

The objective of this study is to rigorously assess the influence of non-ideal instrumental effects on the performance of high-resolution FTIR spectrometers, focusing specifically on the Bruker FTS 120M. Key non-idealities under investigation include retroreflector misalignments, baseline drift, and spectral channeling, which can significantly compromise the accuracy of atmospheric trace gas retrievals. Using advanced diagnostic tools, such as ALIGN60 and LINEFIT, , this study systematically diagnoses and corrects mechanical and optical misalignments under operational conditions. Furthermore, this research addresses existing gaps in the operational protocols of prominent global monitoring networks like the NDACC and the TCCON. By emphasizing the need to integrate real-world instrumental deviations into data analysis frameworks, the study advocates for more robust methodologies that account for practical limitations. Temporal degradation trends, particularly changes in ME and PE, are analyzed to highlight the importance of routine performance evaluations and maintenance schedules for long-term operational stability. By addressing these overlooked challenges, the study ultimately aims to establish standardized methodologies for diagnosing , quantifying, and correcting instrumental artifacts, ensuring that high-resolution FTIR spectrometers, like the Bruker FTS 120M, deliver reliable, reproducible, and precise measurements over time. By addressing these challenges, the research contributes to strengthening the operational frameworks of international networks such as NDACC and TCCON, ultimately advancing global efforts in atmospheric monitoring and climate research.

The paper is structured as follows: Section 2 provides the theoretical and technical background. Section 3 outlines the methodology, followed by the presentation of data analysis results in Section 4. A detailed discussion is presented in Section 5, and the conclusions are summarized in Section 6.

2 Theoretical and Technical Background

2.1 The Ideal FTIR Spectrometer

The Michelson interferometer is a fundamental component of most FTIR spectrometers enabling precise modulation of the OPD between its fixed and movable mirrors or retroreflectors for high-resolution spectral measurements (e.g. Zeng et al. (2022); Zhou et al. (2024)). An ideal FTIR spectrometer, such as the one shown in Figure 1, is characterized by precise and optimized components that ensure high accuracy and reproducibility in spectral measurements. Its retroreflector must be perfectly aligned to maintain a linear OPD, while the beamsplitter requires uniform transmission and reflection properties across all wavelengths to minimize artifacts. Additionally, a high-sensitivity detector and finely tuned amplifiers enhance signal quality, collectively ensuring the reliability of spectral data. Together, these elements produce artifact-free interferograms and high-resolution spectra, achieving a modulation efficiency of unity and eliminating phase errors essential for detailed analysis. When a monochromatic plane wave enters the interferometer, it splits into two beams traveling different paths. Their superposition at the detector forms the DC-corrected interferogram, expressed as

$$I(x) \quad = \quad I(x_0)\cos(2\pi\nu x) \tag{1}$$

where $I(x_0)$ is the intensity at zero path difference, and ν is the wavenumber (e.g. Sahoo et al., 2023). At ZPD, the corner cube mirrors are equidistant from the beamsplitter, causing all incident light to interfere constructively at the detector; as the scan

90 progresses and OPD increases, the interference pattern alternates between constructive and destructive interference based on the source radiation's wavenumber.
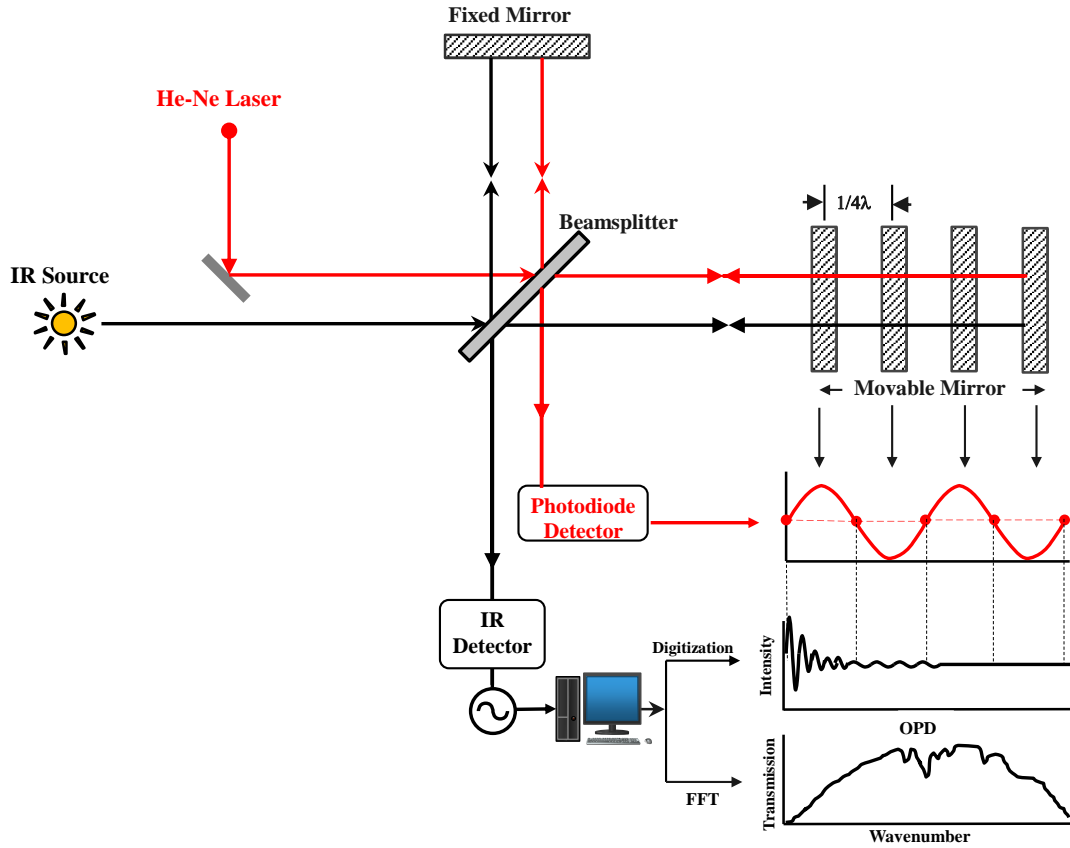
Figure 1. Schematic diagram of an ideal FTIR spectrometer illustrating the working principle, including key components such as the light source, beamsplitter, interferometer, sample chamber, and detector.

2.2 Nominal Instrument characteristic

In practice, an FTIR spectrometer's spectral response deviates from the idealized assumption due to imperfections in components like the beamsplitter, detector, amplifier, and cube-corner retroreflectors (CCRs), (e.g. yuan Yue et al., 2017; Zhang

95 et al., 2018). These components introduce wavenumber-dependent non-uniformities that affect modulation efficiency, which quantifies the ability to encode spectral information accurately (e.g. Hanssen et al., 2022). Realistic interferograms incorporate modulation loss and phase delay:

$$I = \int_{0}^{\infty} S_0(\nu) m(x,\nu) \cos[2\pi\nu x + \phi(x,\nu)] \, d\nu \qquad (2)$$

where $S_0(\nu)$ is the true spectrum, $m(x,\nu)$ is the modulation depth indicating signal quality, and $\phi(x,\nu)$ is the phase error
(e.g. Carnio et al., 2023). These parameters capture the cumulative effects of non-idealities, such as reduced modulation depth
($m(x,\nu)$) and phase distortions ($\phi(x,\nu)$), particularly at higher wavenumbers.

2.2.1 Wavenumber-Dependent Instrument Response

Beamsplitters, such as those made from CaF_2 (e.g. Fig 2(b)), exhibit dispersion that reduces modulation efficiency (e.g. Letz
et al., 2002, 2003). Applying thin germanium coatings ($n = 4.0$) can minimize chirping and enhance performance (e.g. Gill
et al., 2022). The efficiency of a beamsplitter, assuming no absorption or polarization effects, is given by:

$$m_{\mathrm{bs}}(\nu) = 4 \cdot R_{\mathrm{bs}}(\nu) \cdot T_{\mathrm{bs}}(\nu) \tag{3}$$

where R_{bs} and T_{bs} represent reflectance and transmittance. While ideal beamsplitters achieve $m_{\mathrm{bs}} = 100\%$, practical imperfec-
tions, such as surface irregularities and wavelength-dependent absorption, reduce this value. For example, germanium coatings
at a 45° angle of incidence yield an average efficiency exceeding 86% but remain theoretical for perfect uniformity (e.g.
Yenisoy and Tüzemen, 2020).

The liquid nitrogen-cooled InSb detector exhibits peak performance near 4000 cm^{-1}, with modulation efficiency ($m_{\mathrm{det}}(\nu)$)
expressed as:

$$m_{\mathrm{det}}(\nu) = \frac{R_{\mathrm{det}}(\nu)}{R_{\mathrm{det, max}}} \tag{4}$$

where $R_{\mathrm{det}}(\nu)$ and $R_{\mathrm{det, max}}$ are the responsivity at a specific wavenumber and peak responsivity, respectively. The efficiency
decreases from ~ 1 near 4000 cm^{-1} to 0.7–0.8 at 1800 cm^{-1}, necessitating careful calibration (e.g. Shi et al., 2019). Amplifiers
further contribute wavenumber-dependent gain variations due to the properties of resistors and transistors (e.g. Shi et al., 2019).

The CCRs used in the Bruker 120M spectrometer, coated with aluminum, silver, or gold, provide reflectivities exceeding
98% with minimal wavenumber dependence in the mid-IR range, ensuring relatively uniform performance (e.g. Liu et al.,
2019, 2022). Despite these optimizations, component-specific imperfections underscore the need for precise calibration to
ensure high-quality spectral measurements.

2.2.2 Self-Apodization

In typical FTIR spectrometers, it's often assumed that the wave phases of a plane wave (a perfectly collimated beam) do not
exhibit spatial dependence. However, in real-world scenarios, this assumption is challenged by finite-sized sources, such as
extended sources like the sun, which cannot be perfectly collimated due to their finite size (e.g. Wawrzyniuk, 2021). This
introduces spatial dependence to the wave phases across the beam, affecting the modulation function (e.g. Fulton et al., 2015).
Therefore, the total interferogram accounts for the finite divergence angle (α) using a Taylor series expansion of the cosine
function around $\alpha = 0$ and truncating the series to the first two terms (e.g. Ridder et al., 2014; Boone and Bernath, 2019):

$$I(x) = I_0 m_{\mathrm{self}}(\nu,x) cos \left[2\pi\nu x \left(1 - \frac{\Omega}{4\pi} \right) \right] \tag{5}$$
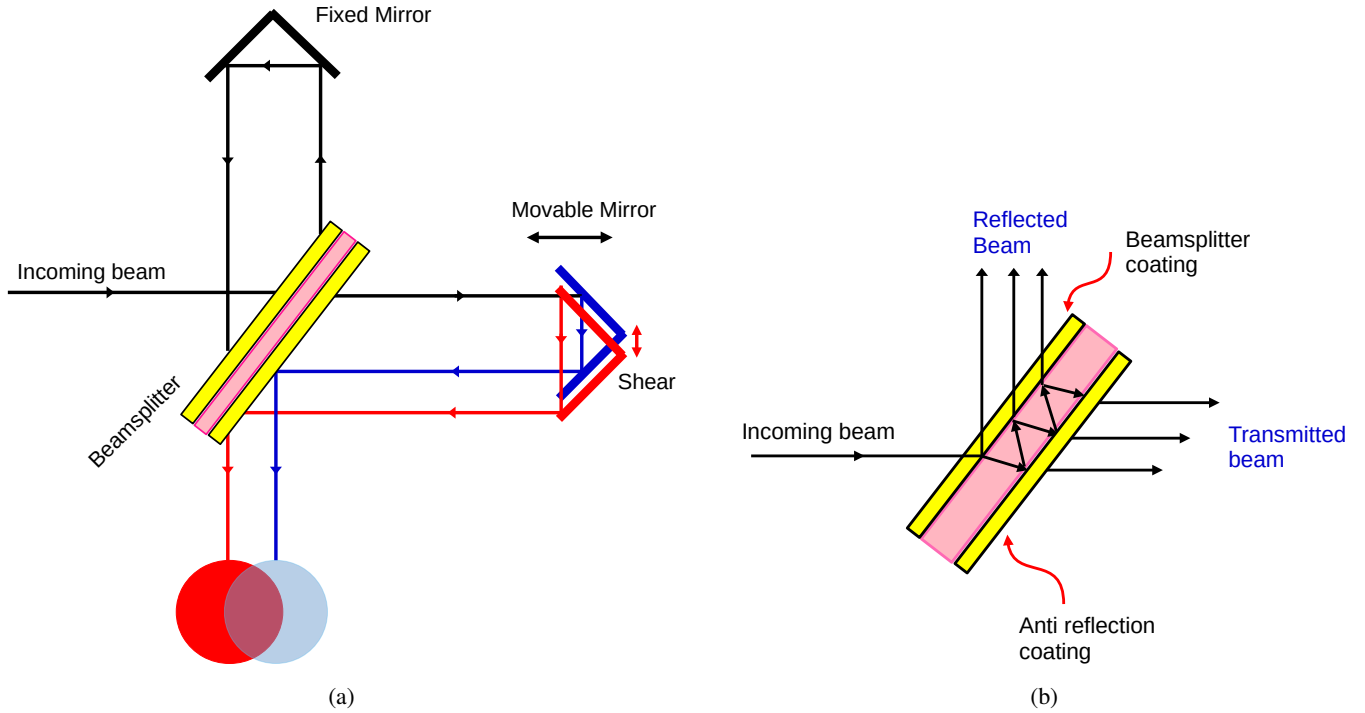
Figure 2. (a) Schematic of the interferometer showing fixed and movable retroreflector mirrors, where one movable mirror is laterally sheared, and light from both mirrors is focused on the detector. (b) Beamsplitter illustrating the partial reflection and transmission of incident light, with the coatings labeled for better visualization.

where Ω is the solid angle of the circular aperture at the focus of a collimating mirror, $\Omega = \pi\alpha^2$ with α representing the angular radius of the field-of-view, and $m_{\text{self}}(\nu, x)$ is the modulation function due to self apodization

$$m_{\text{self}}(\nu, x) = sinc\left(\frac{\Omega\nu x}{2}\right) \tag{6}$$

Hence, there are two effects on the interferogram/spectrum caused by the finite entrance aperture of a non-ideal interferometer (e.g. Gero et al., 2018): the scale/shift change in OPD and wavenumber which can be expressed as

$$\nu' = \nu\left(1 - \frac{\Omega}{4\pi}\right) \quad \text{and} \quad x' = x\left(1 - \frac{\Omega}{4\pi}\right) \tag{7}$$

A perfectly-aligned interferometer will perfectly center the Haidinger fringes on the field stop at all OPDs (e.g. Sun et al., 2018b). The modulation at ZPD is therefore expected to be unity with assumption that our spectrometer is only subjected to unavoidable instrument characteristics (e.g. García et al., 2022). As the mirror moves away from the ZPD, it experiences modulation loss for the fact that tilt are getting worse for the longer OPDs because of the interferometer's FOV (e.g. García et al., 2022; Liu et al., 2021a). For example, a schematic figure (Fig. 3) illustrates the modulation efficiency of a nominally ideal instrument in blue, providing a visual comparison against the theoretical and real instrument performance. For an interferometer

with a cone of radiation of wavenumber ν and solid angle Ω incident upon perfectly aligned mirrors, the interferometer is expected to have tolerable tilt.
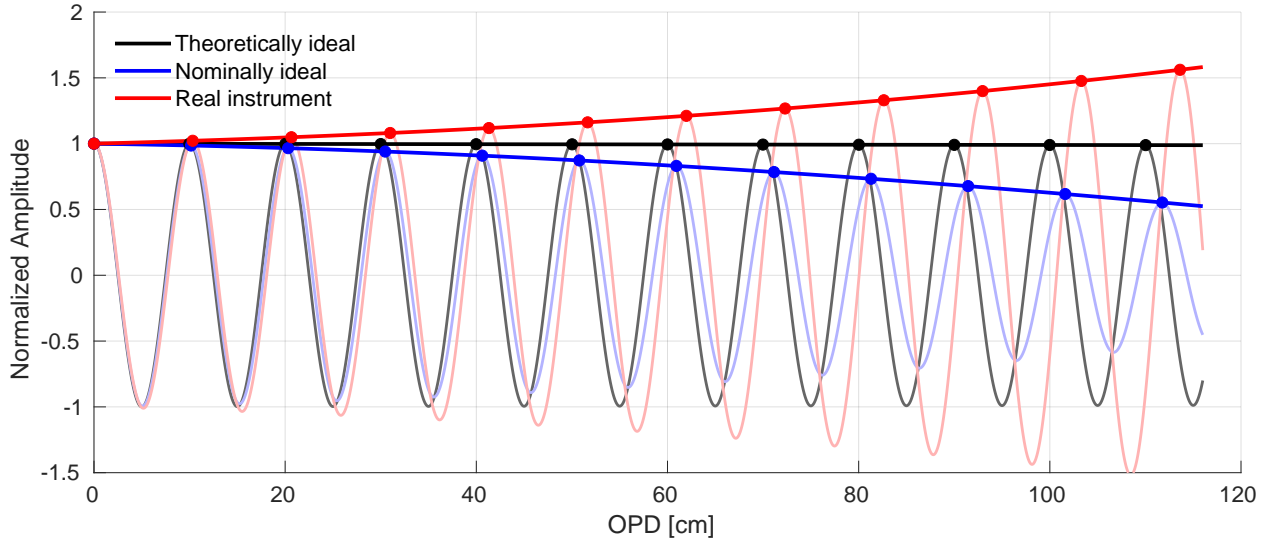
Figure 3. Schematic illustration of the deviation between the ideal interferogram and the measured interferogram, with identification of the characteristics described by the modulation function.

2.3 Fabry-Pérot Etalons

145 The Fabry–Pérot effect, or spectral channeling, occurs due to the interference of light waves undergoing multiple reflections and refractions within parallel optical surfaces (e.g. Ball, 2012; Konevskikh et al., 2015). In FTIR spectrometers, the beamsplitter (e.g. Fig 2(b)) is the primary source of this effect (e.g. Blumenstock et al., 2021). Its layered structure and substrate create Fabry–Pérot cavities that generate standing wave patterns, leading to periodic oscillations in the observed spectrum and reducing the accuracy of spectral analysis (e.g. Blumenstock et al., 2021). When light strikes the beamsplitter, it undergoes 150 partial reflection and refraction at each interface. The transmitted and reflected beams, with decreasing amplitudes due to partial reflection and absorption, are superimposed at the detector. The interference pattern is governed by the optical path length difference (ΔL) between successive transmitted beams, given by (e.g. Hecht, 2016):

$$\Delta L = 2nd\cos\theta, \tag{8}$$

where n is the refractive index, d the thickness of the cavity, and θ the angle of incidence. The phase shift ($\Delta\phi$) associated with 155 this path difference is:

$$\Delta\phi = 4\pi\nu nd\cos\theta, \tag{9}$$

where ν is the wavenumber of light. Constructive interference occurs when: $\Delta\phi = m \cdot 2\pi$ (for integer m), and destructive interference occurs when: $\Delta\phi = \left(m + \frac{1}{2}\right) \cdot 2\pi$. These phase conditions define the periodicity of the spectral oscillations. The

free spectral range (FSR), representing the spacing between constructive interference maxima, is:

$$\nu_{\text{FSR}} = \frac{1}{\Delta L} = \frac{1}{2nd\cos\theta}. \tag{10}$$

160

The intensity of the observed spectrum is affected by these periodic oscillations, which can be modeled as:

$$I(\nu) = I_0(\nu) + A\cos(2\pi f_c \nu + \phi), \tag{11}$$

where $I(\nu)$ is the observed intensity, $I_0(\nu)$ is the true spectrum, A is the amplitude of the channeling oscillations, f_c is the channeling frequency related to the FSR ($f_c = \nu_{\text{FSR}}$), and ϕ is the phase offset. The harmonic oscillations distort the baseline of the spectrum and can overlap with absorption features, making it challenging to accurately retrieve spectral parameters such

165 as line strength, width, and position. These distortions are particularly problematic for weak absorption lines, where the artifact may mimic or obscure real spectral features (e.g. Hecht, 2016; Blumenstock et al., 2021).

2.4 Retroreflector Misalignment and Overmodulation

Bruker interferometers, such as the 120M model, rely on cube-corner retroreflectors to ensure precise and reliable measure-
170 ments. These retroreflectors consist of three mutually perpendicular reflective surfaces forming the corner of a cube, which enables them to reflect incident beams back parallel to their original paths, regardless of the direction of incidence (e.g. Brown et al., 2014). This design minimizes the impact of mirror tilt on the interferometer's performance, maintaining accurate retroreflection even when minor misalignments occur. However, while the cube-corner retroreflector is immune to tilting, it remains sensitive to lateral displacement, where any positional shift can disrupt the beam alignment.

175 Lateral displacement, or shear, becomes a critical factor influencing overmodulation in the interferometer (e.g. Frey et al., 2019). This misalignment introduces an additional OPD that varies with the propagation angle, significantly affecting the modulation depth at the interferometer's center burst (e.g. Martino and Hagopian, 1998; Henault et al., 1999). In the Bruker 120M spectrometer, shear arises from the misalignment of the retroreflector, leading to a lateral shift of the reflected beam in one arm of the interferometer (e.g. Sun et al., 2018b). This shift disrupts phase coherence and reduces modulation depth
180 in the interferogram, particularly at ZPD, due to wavefront aberrations, corner cube retroreflector misalignment, and lateral displacement of optical components (e.g. Yue et al., 2017; Sun et al., 2018b).

To maintain consistency in spectral analysis, the modulation at ZPD is normalized to unity, ensuring proper area-normalization of the ILS (Hase, 2012). While this normalization provides a standard reference, it can introduce an apparent increase in modulation amplitude as a function of OPD in the presence of shear misalignment (e.g. Hase, 2012; Sun et al., 2018b), as evidenced
185 in Figure 3. This apparent increase, however, does not imply a true enhancement of modulation efficiency; rather, it reflects distortions caused by the lateral displacement.

The lateral displacement (Δx) introduced by the misaligned retroreflector can be expressed as:

$$\Delta x = \varepsilon(x)\sin\alpha \tag{12}$$

where $\varepsilon(x)$ is the lateral shift of the retroreflector apex relative to the optical axis, and α represents the acceptable angle of
190 tilt. This displacement introduces phase incoherence between recombining wavefronts, which, for a range of incident angles,

reduces the modulation depth. Studies (e.g. Murty (1960); Kauppinen et al. (2004); Genest and Tremblay (2005)) have extensively analyzed the effects of such lateral shifts on modulation depth. For a circular aperture, these shifts produce a diffraction effect represented by the jinc function:

$$m\left[\nu_0, \varepsilon(x)\right] = \frac{2J_1\left[2\pi\nu_0\varepsilon(x)\alpha\right]}{2\pi\nu_0\varepsilon(x)\alpha} \approx 1 - \frac{\left[2\pi\nu_0\varepsilon(x)\alpha\right]^2}{8} \tag{13}$$

195   Here, J_1 is the first-order Bessel function, and the term $2J_1(x)/x$ represents the diffraction pattern of the circular aperture. As OPD increases, modulation depth decreases due to the worsening effects of shear, emphasizing the need for precise alignment of the retroreflector. Understanding and addressing these misalignments are essential for ensuring accurate spectral measurements and reducing overmodulation artifacts in FTIR spectroscopy.

2.5 Tolerance of Lateral Shift

200   Hase explained that a modulation efficiency greater than unity at maximum OPD indicates shear misalignment, leading to narrower measured lines and decreased accuracy (Hase, 2012). The lateral shift of the moving cube corner causes the greatest decrease in modulation at the ZPD (Kauppinen and Saarinen, 1992). Thus, it is essential to define an acceptable lower limit on the tolerance for lateral displacement of the FTS to maintain the modulation efficiency at the ZPD at an acceptable value. The maximum tolerable shear can be determined when α takes its smallest possible value, which corresponds to the condition for
205   maximum resolution. According to the Jacquinot criterion, the upper limit of the resolving power of the interferometer with the instrumental resolution $\Delta\nu$ is given by (Kauppinen and Horneman, 1991; Kauppinen and Saarinen, 1992):

$$R = \frac{1}{\alpha^2} = \frac{\nu_{\max}}{2\Delta\nu} \tag{14}$$

where $\nu_{\max}$ is the wave number of a monochromatic spectral line. Given that the acceptable modulation at ZPD, $m\left[\nu_0, \varepsilon(0)\right] \geq 0.94$, the above equation gives us an estimate for the maximum acceptable lateral shift of the moving cube corner at the ZPD
210   as follows:

$$\varepsilon(0) \leq \frac{1}{8\pi(\Delta\nu\nu_0)^{1/2}} \tag{15}$$

2.6 Combined Effects of Instrumental Artifacts on the Interferogram

The combined effects of nominal instrument response, misalignment, spectroscopic artifacts, and self-apodization can significantly distort the interferogram in FTIR spectroscopy (e.g. Gero et al., 2018). While the nominal response represents the
215   ideal performance of components, real-world conditions often introduce misalignments that degrade modulation efficiency and induce phase errors. Spectroscopic artifacts further disrupt signal coherence, while self-apodization imposes wavenumber- and OPD-dependent modulation loss due to the finite FOV. These interconnected effects necessitate a comprehensive model that accounts for their cumulative impact, enabling precise corrections and ensuring reliable spectral retrievals. Therefore, by accounting for the instrumental non-idealities, the general expression of the interferogram would take the form:

220    $$I(\nu_0, x) = \frac{1}{2} \times m_{\text{tot}}(\nu_0) \times I(\nu_0)\cos\left[\Delta\phi + \phi_{\text{tot}}(\nu_0)\right] \tag{16}$$

where $m_{\text{tot}}(\nu_0)$ is the total modulation efficiency combining nominal response, misalignment, spectroscopic artifacts, and self-apodization:

$$m_{\text{tot}}(x,\nu_0) = m_{\text{nom}}(x,\nu_0) \times m_{\text{self}}(x,\nu_0) \times m_{\text{shear}}(x,\nu_0) \times m_{\text{spe}}(x,\nu_0) \qquad (17)$$

Here, $m_{\text{nom}}(x,\nu_0)$ represents the modulation efficiency of the spectral response of the nominal instrument such that

$$m_{\text{nom}}(x,\nu_0) = \prod_{i=1}^{N} m_i(x,\nu) \qquad (18)$$

where $m_i(x,\nu)$ represents the modulation efficiency of the i-th component (e.g., beamsplitter, detector, retroreflectors, amplifier), and N is the total number of contributing components. We can simplify further,

$$I(\nu_0,x) = \frac{1}{2} \times m_{bs}(\nu_0) \times m_{op}(\nu_0) \times R(\nu_0) \times G(\nu_0) \times I(\nu_0) \times \cos\left[\Delta\phi + \phi(\nu_0)\right] \qquad (19)$$

where m_{op} is the optical efficiency of the mirrors and m_{bs} is the beamsplitter efficiency, R is the electrical response of the detector to the incident radiation of wavenumber ν_0 and G is the response of the amplifiers and more precisely the filters contained in them. .

Similarly, the phase error $\phi(\nu)$ can be modeled as the sum of phase contributions from individual components:

$$\phi_{\text{tot}}(\nu_0) = \sum_{i=1}^{N} \phi_i(\nu) \qquad (20)$$

where $\phi_i(\nu)$ represents the phase error introduced by the i-th component.

3 Methodology

3.1 Introduction to the Experimental Setup

3.1.1 Historical Perispectives

The Bruker FTS 120M spectrometer, installed in Addis Ababa, is dedicated to measuring atmospheric gases in the mid-infrared (MIR) region and is the only known high-resolution instrument within the NDACC-IRWG network located in the tropical African region. It traces its origins to its predecessor, the Bruker FTS 125HR, originally based in Kiruna, Sweden, where it specialized in near-infrared (NIR) spectroscopy. Following a significant upgrade to enhance its capabilities and shift its focus to MIR spectroscopy, the instrument was renamed the FTS 120M and relocated to Addis Ababa to take advantage of the high-altitude location for improved atmospheric research. In 2009, the Karlsruhe Institute of Technology (KIT) collaborated with Addis Ababa University (AAU) to install the spectrometer at the College of Natural Sciences (9.01° N, 38.76° E, and 2443 m above sea level). Measurements using the instrument began in May 2009, and since then, research studies have been conducted by KIT-affiliated researchers as well as researchers and graduate students from the university (e.g. Takele Kenea et al., 2013; Tsidu et al., 2014; Hase et al., 2015; Yirdaw Berhe et al., 2020; Berhe et al., 2020).
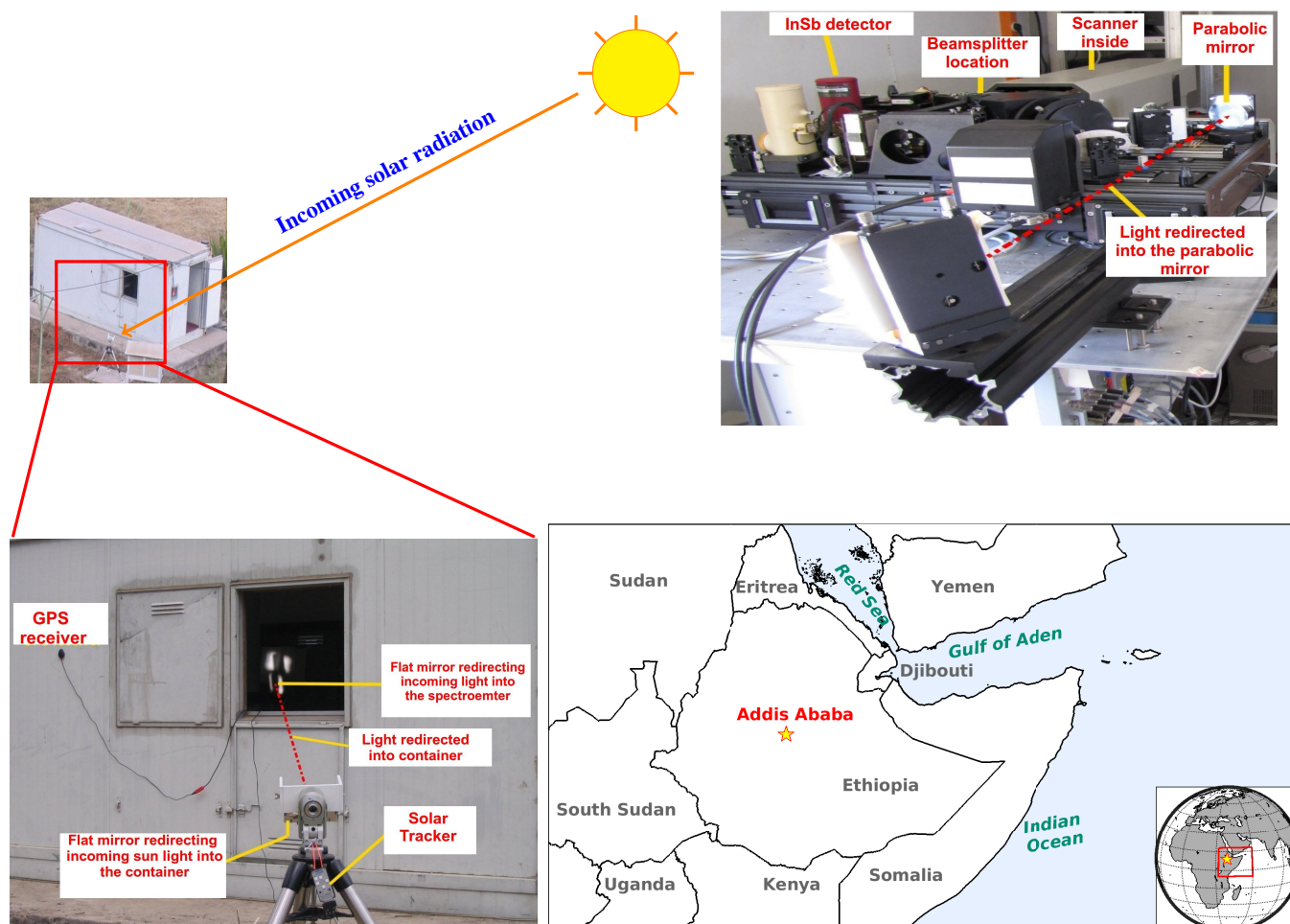
Figure 4. Deployment and configuration of the Bruker 120M spectrometer in Addis Ababa. The instrument is installed at Addis Ababa University, College of Natural Sciences (red star on map). The lower-left panel shows the container setup with a GPS antenna for time synchronization and a solar tracker redirecting sunlight into the spectrometer. The top-right panel displays key components of the instrument, including the InSb detector, beamsplitter, scanner, and parabolic mirror. The sun and arrows illustrate the path of incoming solar radiation.

3.1.2 Overview of the Components

The Bruker FTS 120M spectrometer in Addis Ababa is equipped with advanced components designed to optimize its performance for high-resolution atmospheric measurements. Central to its operation is a helium-neon (HeNe) laser, which ensures precise alignment and stability of the scanning mirror, critical for producing accurate spectral data. The spectrometer utilizes a CaF_2 beamsplitter, covering the spectral range of 1200-15000 cm^{-1}, paired with a liquid-nitrogen-cooled indium antimonide (InSb) detector to capture interferograms in the MIR region. Although the system also supports a KBr beamsplitter for the 450-4800 cm^{-1} range and a Mercury Cadmium Telluride (MCT) detector, these components have not been utilized at this site. The system operates under a vacuum maintained at pressures below 1 hPa by a dedicated pump, minimizing atmospheric interference and enhancing stability. Significant maintenance in 2012 by the KIT addressed an InSb detector failure and extended the optical path length to improve spectral resolution. Manufactured by Bruker Optics in Germany, the FTS 120M offers exceptional sensitivity and resolution, making it an integral tool for atmospheric research and a key instrument in global networks such as NDACC and TCCON.

Filter number	Wavenumber range (cm^{-1})
1	3950 - 4900
2	2900 - 3950
3	2400 - 3320
4	1900 - 2750
5	1730 - 2250

Table 1. NDACC narrow bandpass filters used in Bruker 120M at Addis Ababa

3.2 Measurements Conditions

The operation of the Bruker FTS 120M spectrometer is carefully managed under controlled environmental conditions to ensure high performance and precise data acquisition. The spectrometer room is maintained within a temperature range of 18°C to 35°C, with temperature fluctuations strictly limited to no more than 1°C per hour and 2°C per day (Bruker Optik GmbH, 2009). These limits are critical to prevent thermal gradients within the instrument, which could lead to mechanical distortions in the optical components, adversely affecting alignment and spectral resolution. Relative humidity is kept below 80% to protect hygroscopic elements, such as the KBr beamsplitter, optical filters, and sample cell windows, from moisture-induced degradation. To avoid condensation effects, the room temperature is maintained slightly above the ambient level. Additionally, the InSb detector operates in a vacuum environment with pressures below 1 hPa, which minimizes thermal noise and enhances sensitivity. The vacuum pump is required periodically to maintain these low-pressure conditions, particularly after maintenance activities or when the system indicates pressure levels exceeding the operational threshold, ensuring the detector continues to

function with optimal performance. Together, these environmental and operational controls are vital for maintaining instrument stability and enabling high-resolution measurements essential for precise atmospheric trace gas retrievals.

3.3 ILS Characterization

3.3.1 Background Signal Characterization

275 Background signal measurements were conducted with a high-precision configuration optimized for MIR spectral analysis. The system employed a CaF_2 beamsplitter and a liquid nitrogen-cooled indium antimonide (LN-InSb) detector with a 30° FOV. The aperture was set to 0.85 mm, and the source was configured for MIR emissions. A focal length of 220 mm was used to focus the optical path. Signal processing included no high-pass filter, a low-pass filter with a cutoff at 20 Hz, and optical filters configured as Filter 3 for both primary settings, with an open configuration for additional filtering. A preamplifier gain

280 of 1 was applied, and acquisition was performed in single-sided, forward-backward mode, with 100 scans (50 forward and 50 backward) completed over ~ 68 minutes. The interferogram was obtained at a resolution of 0.00775 cm^{-1}, phase corrected using the Mertz algorithm (e.g. Chen et al., 2024), and stored in the OPUS software as full bidirectional data (e.g. Lingling et al., 2017), preserving both forward and backward scans (e.g. Figure 5(a)). The forward and backward interferograms were transformed and phase corrected separately, with the resulting spectra combined using a mean function (e.g. Figure 5(b)). The

285 zero crossings of the HeNe laser, used to sample the interferogram, were calculated based on the Nyquist theorem (e.g. Zabit and Bernal, 2023), which ensures adequate sampling by setting the maximum detectable frequency (ν_{max}) to half the sampling rate. Using the relationship:

$$\Delta x = \frac{1}{2(\nu_{\text{max}} - \nu_{\text{min}})} \tag{21}$$

where Δx is the sampling interval of the laser, and ν_{min} is the minimum frequency (set to 0 in this case). With ν_{max} derived

290 from the spectral range, the sampled positions ($x_{\text{HeNe\_sampl}}$) were calculated as:

$$x_{\text{HeNe\_sampl}} = [0, \Delta x, 2\Delta x, \dots, (N-1)\Delta x] \tag{22}$$

where N is the total number of interferogram data points. This approach ensured accurate mapping of the interferogram to spectral data. The apodization function used was Boxcar, and the system was calibrated with a He-Ne laser at $\sim$15,800 cm^{-1}.

3.3.2 Low-Pressure Gas Cell Measurements

295 The NDACC-IRWG enforces rigorous standards for ILS characterization and correction to ensure consistent, accurate, and reliable spectroscopic measurements across its global network of FTIR instruments. The ILS, which defines the instrument's response to a monochromatic light source, is regularly evaluated through established methods such as low-pressure HBr gas cell measurements and He-Ne laser-based interferometry to assess key parameters, including modulation efficiency, phase errors, and line broadening (e.g. Hase et al., 1999; Hase, 2012). These evaluations ensure compliance with predefined thresholds

300 to minimize spectral distortions and retrieval inaccuracies. Identified deviations are addressed through corrections integrated
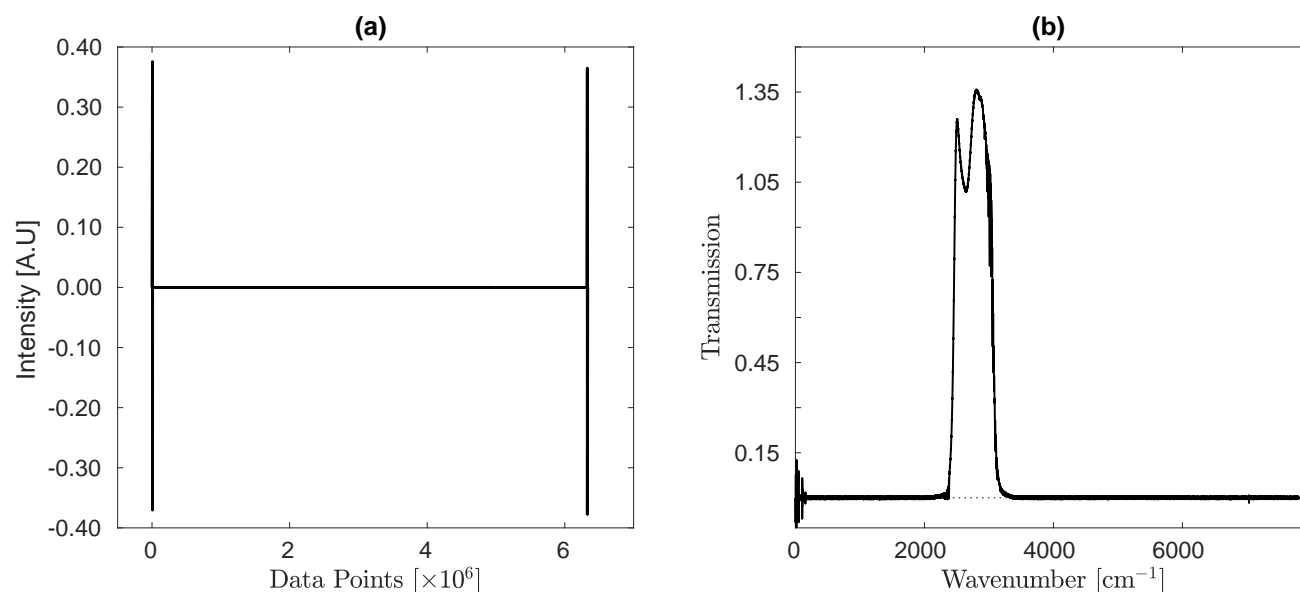
Figure 5. (a) Single-sided, bi-directional interferogram from the measurement dated 091209 and (b) its corresponding Fourier transform. The interferogram was obtained at a resolution of 0.00775cm⁻¹ using 100 scans. Phase correction and spectrum calculation were performed using the Mertz method. Forward and backward scans were individually transformed, phase-corrected, and combined using a mean function.

into retrieval algorithms and routine hardware maintenance, including optical realignments and field stop optimizations. Environmental stabilization measures, such as thermal control and vibration isolation, further improve fluctuations (e.g. García et al., 2022).

The calibration of the Bruker IFS 120M spectrometer relies on low-pressure HBr gas cells, which provide narrow Doppler-
305 broadened absorption lines that are highly sensitive to optical misalignments and imperfections. These features, combined with the closely spaced absorption lines ($\sim$ 20 cm⁻¹ apart), (Gupta et al.) and the presence of the isotopologues H^{79}Br and H^{81}Br, double the number of calibration lines, enabling detailed spectral analysis. Measurements employed similar instrumental settings as those used for background signal acquisition, ensuring consistency in aperture and optical configurations, and focused on the spectral range of 2408.0-2530.0 cm⁻¹. A 2 cm sealed glass cell filled with HBr at 1.5 mbar, in accordance with
310 NDACC-IRWG standards, was used to identify instrumental artifacts, including baseline offsets, phase errors, and spectral channeling, as well as to evaluate modulation efficiency and validate the spectrometer's response. The transmittance spectrum was calculated using OPUS software by dividing the sample spectrum by the background, effectively minimizing artifacts such as water vapor absorption. The resulting spectrum revealed distinct P-branch (P(5) to P(8)) and R-branch (R(4) to R(7)) lines dominated by Doppler broadening, with excellent agreement between measured and simulated data, as shown in Figure
315 6(a). Residuals between the measured and calculated spectra provided valuable insights into misalignment and spectroscopic artifacts, highlighting the importance of regular HBr cell measurements and residual analysis using LINEFIT 14.5 software to ensure instrument accuracy and reliable spectroscopic data, as noted by (Hase et al., 1999; Hase, 2012).
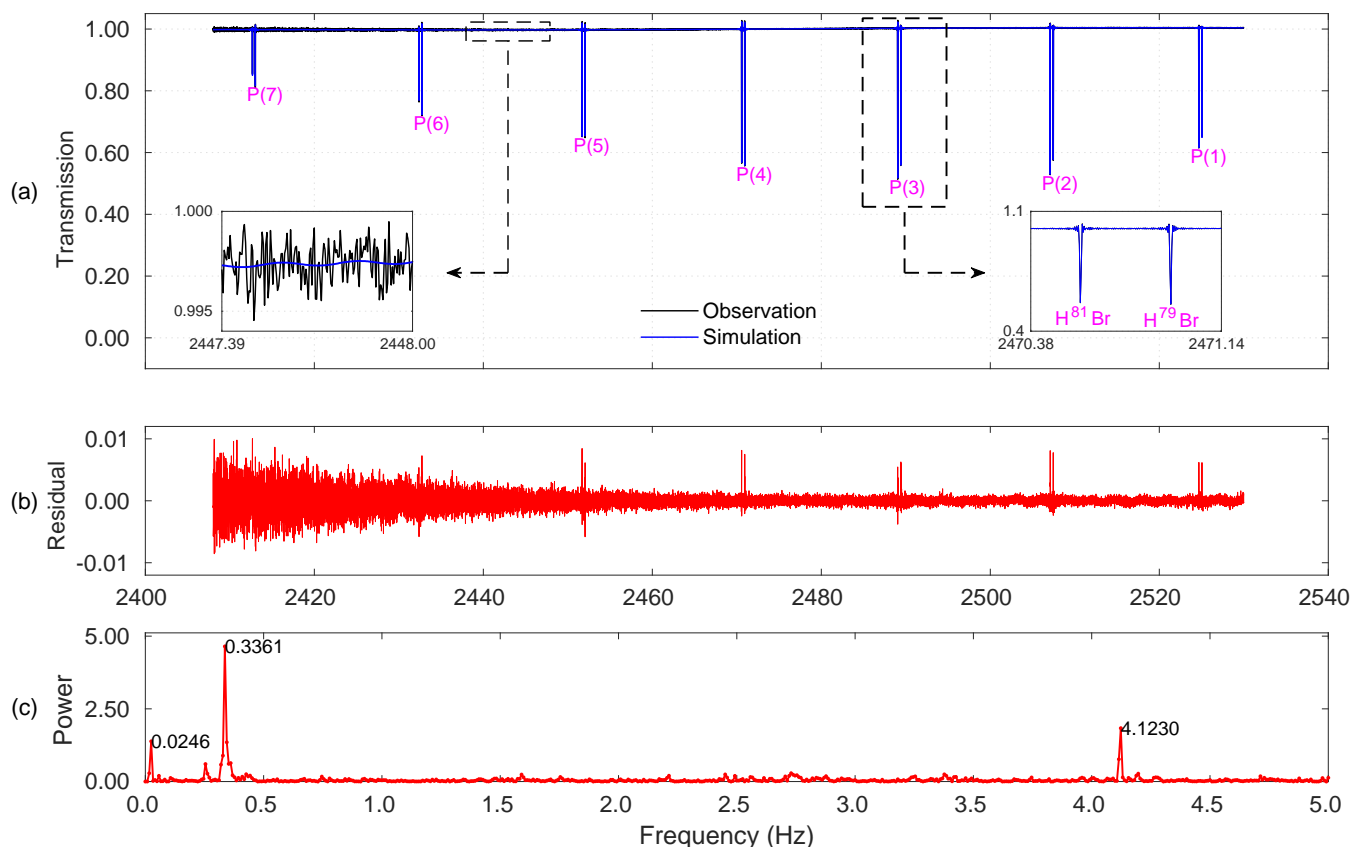
Figure 6. HBr transmission spectra acquired via gas cell measurement. (a) Comparison between observed and simulated spectra in the region 2400-2540 cm^{-1}, illustrating P-branch transitions. Insets display isotopic splitting (right) and low-amplitude channeling patterns (left). (b) Residuals between experiment and simulation. (c) FFT of the residual showing dominant frequencies linked to channeling artifacts arising from instrumental imperfections. Data acquired on 121214.

3.4 True gas cell column amount

Ideally, it was assumed that the temperature of the room was identical to that of the HBr cell, and that the pressure within the
320 HBr cell remained constant throughout the experiment. Thus, the amount of the gas sample contained inside the cell can be drived from the consideration of the ideal gas law and initial cell parameters (e.g. Tenny and Cooper, 2017):

$$\text{cell column} = 7.243 \times 10^{24} \left(\frac{P\ell}{T} \right) = 7.39 \times 10^{20} \frac{\text{molecules}}{m^2} \tag{23}$$

Where P and T are the pressure in millibar and the temperature in Kelvin of the HBr gas confined inside the cell, respectively and ℓ is the thickness of the HBr cell.

325 However, uncertainty in the calculation of the actual gas concentration in the cell arises from the temperature of the gas cell and imperfections encountered in the intsrument optics. Though the temperature of the room is a constantly monitored

quantity, it may not be representative of the actual mean temperature of the absorbing HBr (e.g. Alberti et al., 2022). The temperature of the room and the temperature within the cell may differ slightly due to several factors. For example, the cell's environment, influenced by the presence of the HBr gas and its interaction with the cell material, could lead to slight variations

330 in temperature. The effective temperature of the gas is therefore determined by least-squares fit of the retrieved line strengths. Moreove, HBr cells are known to experience slow leakage over time, which results in a gradual decrease in both concentration and pressure (Lutsch, 2019). Consequently, it becomes essential to accurately determine the HBr column amount and pressure to ensure the reliability of experimental data.

LINEFIT has been effectively utilized to retrieve the total pressure, partial pressure, and cell column amount under specified

335 conditions, as summarized in Table 2. Initially, the temperature, pressure, and total pressure from an ideal instrument setup were used as starting parameters for the LINEFIT run. The process began by fitting the temperatures of the two isotopes of HBr gases within the cell, continuously updating the cell column as the temperature fluctuated until the temperature differences between the isotopes stabilized. Subsequently, with the fitted temperature constant, both the partial and total pressures were varied, and the cell column was updated to reflect these new pressures until the column ratio between the isotopes approached

340 1:1. For enhanced accuracy, further refinement was conducted by iterating with the total pressure, ensuring it remained greater than the partial pressure. The cell pressure was repeatedly updated based on the retrieved concentration until it converged with a defined threshold of 0.001 mbar, ensuring precise and reliable results.

Dates [YYMMDD]	Scanner Temperature [Kelvin]	Partial Pressure [millibar]	Total Pressure [millibar]	Temperature [Kelvin]	Column [$\times 10^{20} \frac{molecules}{m^2}$]
091208	297.65	1.50	1.51	298.6	7.33
100128	299.25	1.40	1.50	301.7	7.20
110117	294.95	1.50	1.60	298.7	7.76
121214	296.35	1.50	1.62	296.8	7.91
130218	298.05	1.50	1.58	300.3	7.62
150317	292.75	1.40	1.50	295.6	7.35
161021	291.35	1.40	1.49	293.1	7.36

Table 2. LINEFIT retrieval of cell temperature, cell column amount, partial pressure and total pressure of the HBr istopes.

3.5 LINEFIT14.5

Retrieval of the ILS is a critical step in evaluating the performance of FTIR spectrometers. In this study, the LINEFIT software,

345 developed by Hase et al. (1999)., was employed to retrieve the ILS parameters. LINEFIT is a flexible tool that supports both simplified parameterization for near-ideal instruments and detailed descriptions for significantly non-ideal conditions (e.g. Alberti et al., 2022). It retrieves the ILS by characterizing two primary distortions: ME, which quantifies the attenuation of

modulated radiation, and PE, which represents asymmetry in the line shape caused by phase shifts in the optical components. These distortions are influenced by instrumental factors, including baseline drift, spectral channeling, and spectral shifts, which
350   arise from optical misalignments and calibration errors. LINEFIT provides two parameterization schemes: a simple parameter set, using a linear decline in ME and a constant PE, and an extended parameter set, which employs 40 parameters to capture variations in ME and PE across the interferogram with smoothness constraints ensuring physical realism. Input data included absorption lines selected from microwindows with spectroscopic properties derived from the HITRAN database. Gas cell parameters, such as pressure, temperature, and column density, were carefully controlled to achieve Doppler-limited linewidths
355   and precise spectral profiles. Through iterative adjustments, LINEFIT minimizes residuals between the measured and simulated spectra, offering a comprehensive characterization of both ideal and non-ideal instrument behavior.

3.6   ALIGN60

ALIGN60 is a model included in the LINEFIT package that calculates the instrument ILS and Haidinger fringes based on misalignment parameters, such as retroreflector displacement or aperture shifts, to evaluate and correct interferometer perfor-
360   mance. The model has been used in previous studies (e.g. Sun et al., 2018a, b; Yin et al., 2021) and its simulation results have been found to be reliable for evaluating and correcting interferometer performance. According to Sun et al. (2018b), the optical misalignments on high-resolution FTIR spectrometers can be modelled as:

$$\varepsilon(x) = C_0 + C_1 \cdot \mathrm{x} + C_2 \cdot \cos\left(\frac{2\pi \cdot \mathrm{x}}{\mathrm{T}}\right) + C_3 \cdot \sin\left(\frac{2\pi \cdot \mathrm{x}}{\mathrm{T}}\right) \tag{24}$$

where C_0 represents the constant shear offset, C_1 describes the linear shear dependence, and C_2 and C_3 capture periodic
365   components arising from mechanical bending or oscillations in the retroreflector system. By incorporating both constant and periodic shear contributions, ALIGN60 provides a comprehensive simulation of their effects on interferometric measurements. Additionally, it models decentering of the field stop, boundary sharpness, and deformation of the field stop image, further influencing fringe patterns. By generating sketches of laser fringes at specific OPD positions, ALIGN60 allows for the visualization of phase distortions and their influence on Haidinger fringes. These simulations are critical for diagnosing mechanical
370   misalignments, optimizing instrument performance, and improving the accuracy of atmospheric trace gas retrievals.

3.7   Simulating Nominal Haidinger Fringe

The determination of the Haidinger fringe period and its simulation involved a systematic approach to assess its impact on instrument performance. The period of the shear was calculated by analyzing the phase error data from LINEFIT under the nominal configuration. First, the phase error was subjected to a FFT to identify the dominant periodic components. The am-
375   plitude spectrum resulting from the FFT was sorted in descending order, and the frequency corresponding to the maximum amplitude was identified as the dominant shear frequency. The period of the shear was then determined as the reciprocal of this frequency, enabling precise characterization of the periodic misalignment.

The simulation of the ILS using ALIGN60 was performed to replicate the effects of the Haidinger fringe and validate the findings against LINEFIT results. Visual inspection of the modulation efficiency pattern from the Bruker 120M spectrometer

380   at our site revealed similarities to the cosine bending misalignment category described in Sun et al. (2018b). Based on this

observation, a periodically varying cosine bending misalignment was assumed, with the initial amplitude set according to the

values reported in prior studies (e.g. Sun et al., 2018b). ALIGN60 was configured to simulate the ILS at grid points matching

those used in LINEFIT to ensure consistency.

     To quantify the agreement between the ILS simulated by ALIGN60 and LINEFIT, the following objective function was

385   used:

$$\text{Objective Function} = \sqrt{\text{mean}\left[(\text{ILS}_{\text{ALIGN60}} - \text{ILS}_{\text{LINEFIT}})^2\right]} \tag{25}$$

The amplitude of the misalignment was iteratively tuned to minimize this objective function. Convergence was achieved when

the RMSE between ALIGN60 and LINEFIT fell below 0.1. Once the optimized misalignment parameters were established,

the final ILS simulation was performed using ALIGN60, providing a robust characterization of the Haidinger fringe effects on

390   the spectrometer's performance.

3.8 ILS Retrieval Algorithm Configuration

The simulation of solar spectra was performed using two configurations: a nominal setup representing ideal conditions and a

misaligned setup reflecting realistic instrument deviations. In the LINEFIT ILS retrieval, the nominal configuration assumed

zero offsets, no wavenumber shifts, and excluded spectral channeling. The misaligned setup introduced deviations, starting with

395   the nominal baseline as an initial guess while initially excluding channeling. For baseline correction, a sixth-degree polynomial

was chosen to model complex variations without overfitting, expressed as:

$$y_i = a_0 + \sum_{j=1}^{k} \left(a_j \nu_i^j + e_j\right) \tag{26}$$

where y_i is the baseline-corrected transmittance spectrum, ν_i is the wavenumber, a_0 is the offset, a_1 the slope, a_2 the curvature,

and higher-degree terms (a_3 to a_6) account for additional baseline distortions. The coefficients were determined using least-

400   squares regression, and the corrected baseline was iteratively subtracted to obtain distortion-free spectra.

     In the analysis of transmittance spectra, the observed intensity, which is often contaminated by spectral channeling, is

effectively handled by LINEFIT through the decomposition of the channeling component into its sine and cosine projections.

The channeling term, represented as $A\cos(2\pi f_c\nu + \phi)$, is decomposed into $A\cos\phi\cos(2\pi f_c\nu) + A\sin\phi\sin(2\pi f_c\nu)$. This

allows the observed intensity to be expressed in summation form as:

405   $$I(\nu) = I_0(\nu) + \sum_{i=1}^{N} \left[A_{\text{cos},i}\cos(2\pi f_i\nu) + A_{\text{sin},i}\sin(2\pi f_i\nu)\right], \tag{27}$$

where N is the total number of channeling frequencies considered, and $A_{\text{cos},i}$ and $A_{\text{sin},i}$ are the amplitude projections along the

cosine and sine components for the i-th channeling frequency f_i. These projections are related to the amplitude A_i and phase

ϕ_i of the i-th channeling component by the equations:

$$A_{\text{cos},i} = A_i \cdot \cos(\phi_i), \quad A_{\text{sin},i} = A_i \cdot \sin(\phi_i), \tag{28}$$

410   and the overall amplitude A_i and phase ϕ_i are reconstructed as:

$$A_i = \sqrt{A_{\cos,i}^2 + A_{\sin,i}^2}, \quad \phi_i = \tan^{-1}\left(\frac{A_{\sin,i}}{A_{\cos,i}}\right). \tag{29}$$

The amplitude and frequency of the channeling spectra were identified using a FFT applied to the residuals between the calculated and observed HBr spectra, transforming the data from the wavenumber domain to the frequency domain as shown in the Figure 6(b). Initially, an ideal instrument state was assumed in the LINEFIT software, setting the amplitude and frequency

415   of channeling spectra to zero. The FFT results provided initial estimates for these parameters, which LINEFIT iteratively refined to accurately determine their values. Once the baseline fitting process converged, the channeling parameters were further adjusted, resulting in an ILS profile that reflected the spectrometer's non-ideal characteristics. LINEFIT also eliminated the channeling spectra, ensuring these artifacts did not interfere with the analysis of the transmittance spectra. The general workflow, encompassing the entire experimental setup, data processing, and iterative analysis, is illustrated in the figure 7.

420   ## 3.9   Performance Evaluation Metrics

To compare the performance of the nominal and modified configurations, several metrics were used to evaluate the quality of the spectral simulations. These metrics focus on the residuals, which represent the difference between the observed and simulated spectra, and provide a quantitative assessment of the simulation's accuracy. The following equations define the metrics used in this study:

Maximum Residual: $\text{Max Residual} = \max\left(|r_i|\right)$

Residual Range: $\text{Residual Range} = \max\left(r_i\right) - \min\left(r_i\right)$

425   Standard Deviation: $\sigma = \sqrt{\frac{1}{N-1}\sum_{i=1}^{N}\left(r_i - \bar{r}\right)^2}$

Mean Absolute Error: $\text{MAE} = \frac{1}{N}\sum_{i=1}^{N}|r_i|$

Root Mean Square: $\text{RMS} = \sqrt{\frac{1}{N}\sum_{i=1}^{N} r_i^2}$

Correlation Coefficient: Pearson correlation coefficient

These metrics were applied systematically to quantify the differences between observed and simulated spectra. By focusing on residuals, the analysis captured the variations introduced by instrumental non-idealities and highlighted the improvements achieved in the modified configuration. This evaluation forms the basis for understanding the effectiveness of corrections applied to the spectrometer's setup.

430   The signal-to-noise ratio (S/N) measures the strength of a signal relative to background noise, offering an essential metric for assessing spectral data quality. For the P(6) line in the HBr transmittance spectrum, the S/N was calculated by:

$$\text{S/N} = \frac{S}{\sigma_{\text{noise}}}$$
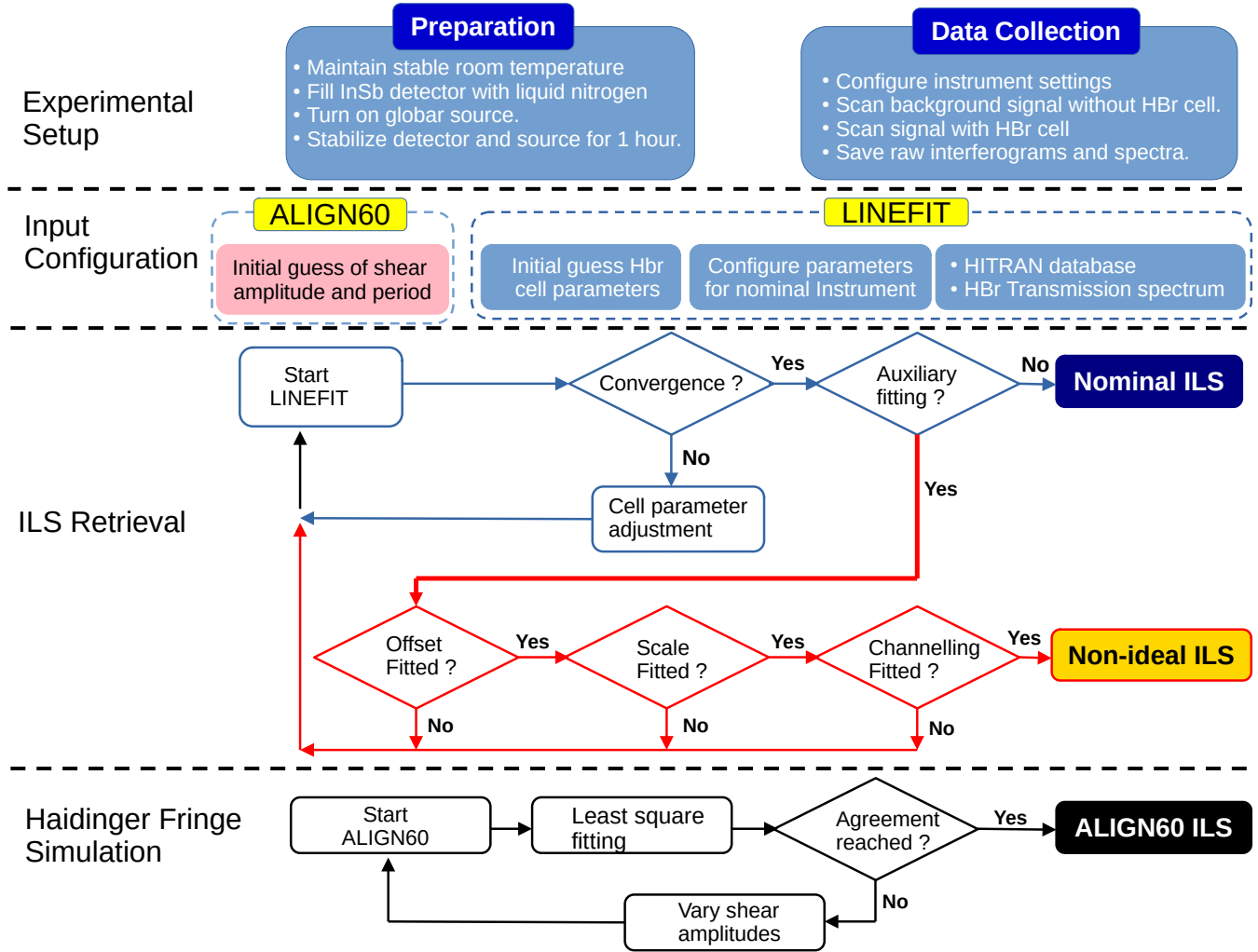
Figure 7. Workflow for Instrumental Characterization: integrating experimental setup, data Processing with LINEFIT and ALIGN60, and iterative optimization for ILS and Haidinger Fringe Simulations.

where S represents the mean of the fitted signal in the region of interest, and σ_{noise} denotes the RMS of the residuals, obtained after subtracting a linear fit from the measured spectrum over the same interval. This approach provides a more accurate

435   estimate of random noise by first accounting for the underlying signal trend.

Asymmetry of the ILS is an important characteristic for evaluating deviations from an ideal symmetric profile. For a line shape with side lobes, the asymmetry can be assessed by comparing the heights of the first side lobes on either side of the central peak. We calculated the asymmetry as the magnitude of the height difference between the two first side lobes, normalized to the height of the central peak. Mathematically, the asymmetry is given by (e.g. García et al., 2022):

440
$$A_{\mathrm{ILS}} = \frac{|H_{\mathrm{left}} - H_{\mathrm{right}}|}{H_{\mathrm{peak}}}$$

where H_{left} is the height of the first side lobe on the left side of the central peak, H_{right} is height of the first side lobe on the right side of the central peak and H_{peak} is the height of the central peak.

The Full Width at Half Maximum (FWHM) of the ILS was calculated by determining the positions where the ILS crossed half of its maximum intensity. Linear interpolation was used between adjacent data points to estimate the exact crossing
445 positions. The FWHM was then computed as:

$$\text{FWHM} = x_{\text{right}} - x_{\text{left}}$$

where x_{left} and x_{right} represent the positions on either side of the central peak where the ILS crossed the half-maximum threshold.

To analyze the rate of change of the ILS, its first derivative was calculated numerically. The derivative was computed using
450 the finite difference method:

$$\frac{d\text{ILS}}{dx} \approx \frac{\Delta\text{ILS}}{\text{step}}$$

where ΔILS is the difference between consecutive points in the ILS data, and step is the sampling interval along the x-axis. This derivative provides insight into the slope and behavior of the ILS, particularly around the peak and side lobes.

To quantify the relative deviation between modified and measured values of the ILS or other metrics such as σ and RMS,
455 we calculated the percentage difference. The formula used is:

$$\text{Percentage Difference} = \frac{M_{\text{modified}} - M_{\text{measured}}}{M_{\text{measured}}} \times 100$$

where M_{modified} is the value of the metric under modified configuration and M_{measured} is the value of the metric under nominal (measured) conditions.

4 Results and Data Analysis

460 The figures shown in the Fig. 8 - 11 illustrate the progressive degradation of the FTIR instrument's performance over time, based on data collected from 091208 to 161021. Figure 8, generated from the background measurement and apodized using the boxcar apodization function, shows a clear decline in interferogram intensity for both forward and backward scans, particularly near the ZPD. This reduction highlights the increasing impact of retroreflector misalignment, source brightness fluctuations, and the aging of optical components. Figure 10 provides a detailed view of the ZPD region, showing diminished intensity
465 and growing variability in sampling points over time, particularly in later scans like 150317, reflecting alignment instability. Figure 9, which includes 512 sampling points with a broken x-axis for clarity, reveals increasing discrepancies between forward and backward scans, suggesting mechanical drift and optical misalignments. Figure 11 illustrates the evolution of the real and imaginary components of the complex interferogram intensity at the ZPD and its maxima. Over time, both components decline significantly, with the 3rd maximum showing the greatest reduction in scans such as 150317 and 161021. These
470 observed degradations, stemming from alignment and component issues, impact the modulation efficiency and phase accuracy, influencing the overall quality of spectral data and emphasizing the need for regular instrument maintenance and recalibration.
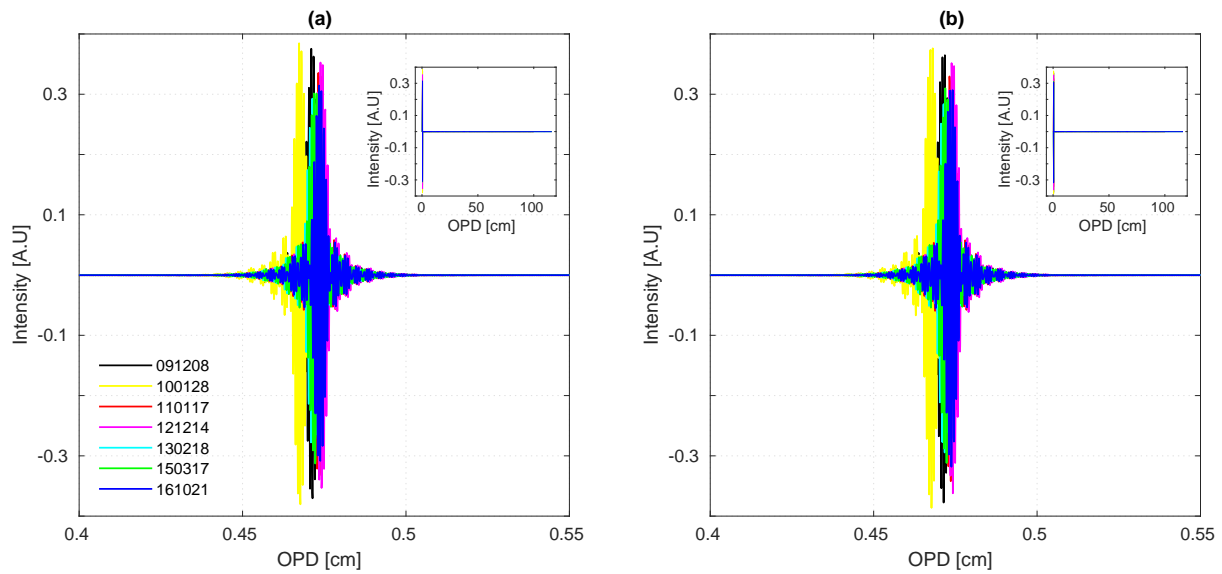
Figure 8. Apodized raw interferograms from background measurements using the boxcar apodization function, showing (a) forward scans and (b) backward scans, illustrating the evolution of intensity over time from 091208 to 161021, with noticeable degradation near the ZPD.
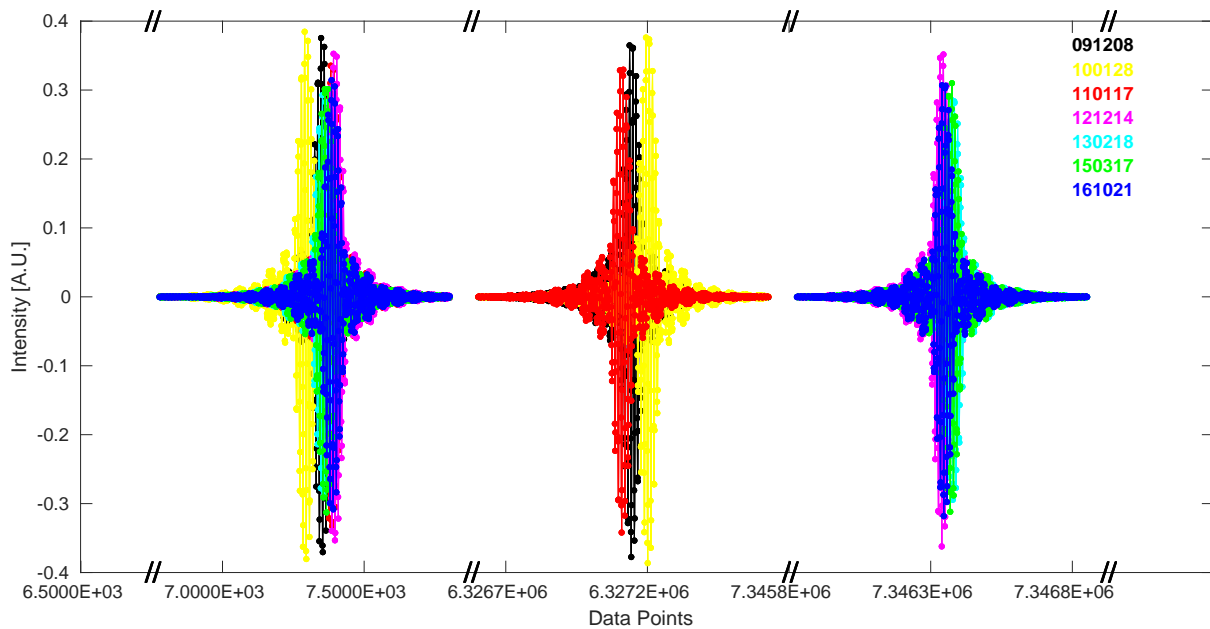
Figure 9. Sampling point analysis of apodized raw interferograms with 512 data points plotted for both forward scans and backward scans, with a broken x-axis for better visualization.
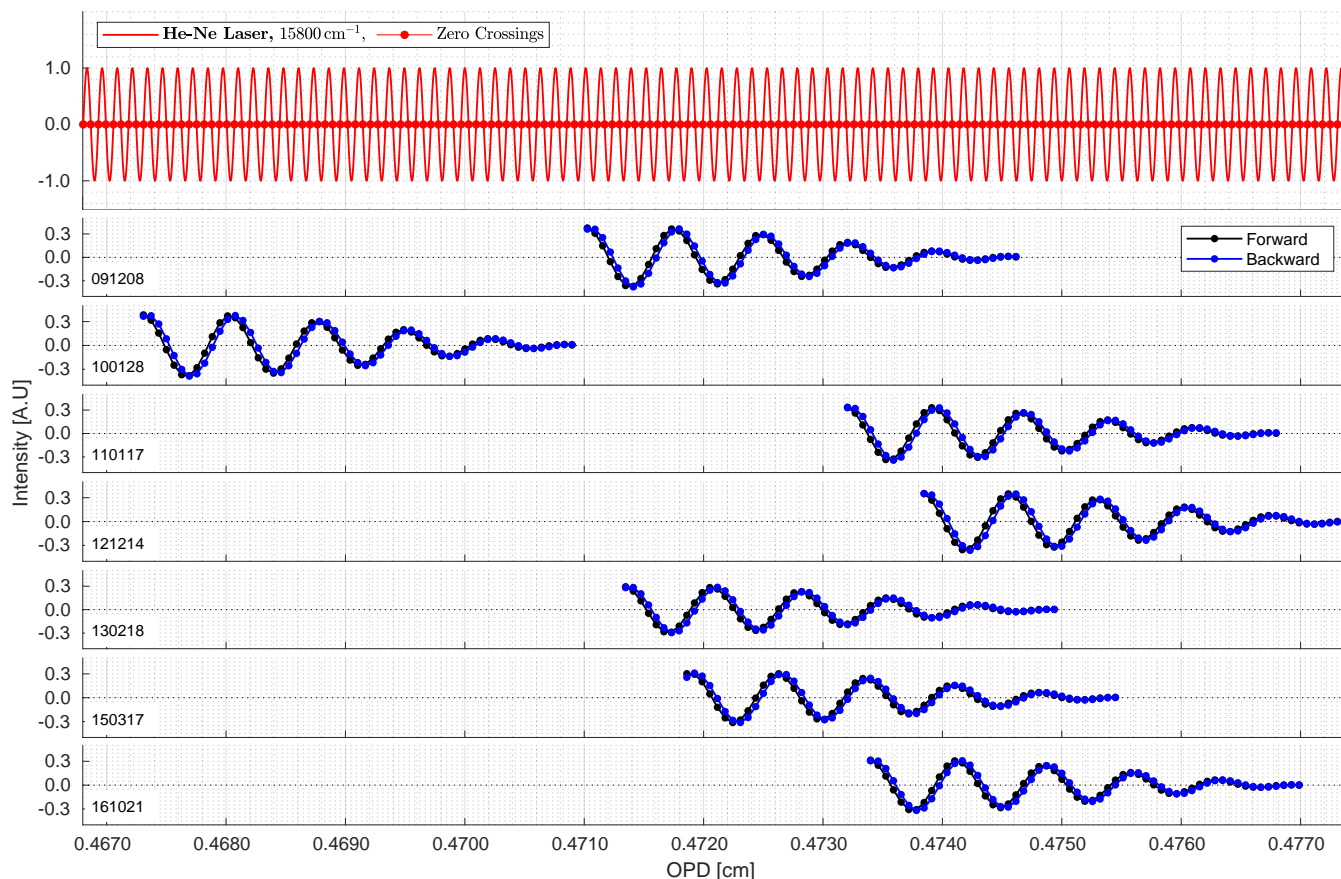
Figure 10. Zoomed view of the apodized raw interferograms near the ZPD for background measurements, showing both forward scans and backward scans. The figure includes the simulation of He-Ne laser reference signal at 15800 cm^{-1} and its zero crossings, which serve as a timing reference for sampling.

The HBr transmission spectra presented in Figure 13 demonstrate high correlation coefficients ($R^2 > 0.99$) for both the nominal and modified configurations, indicating strong agreement with the observed spectra across all dates. However, the modified configuration consistently achieves slightly higher fidelity in capturing instrumental characteristics, as evidenced by

475   its improved residual behavior. This is particularly apparent in the residual analysis, where the nominal configuration displays greater variability and higher error metrics across all cases. In contrast, the modified configuration yields systematic reductions in residual range, σ, and MAE, with improvements as high as 5–6% on challenging dates such as 150317 and 161021. On 150317, for example, the residual MAE improves from 0.0849×10^{-2} to -5.9211%, and the range shifts from 2.0941×10^{-2} (nominal) to -2.5109% (modified), reflecting the impact of correction. Similarly, the maximum residual difference

480   on 121214 increases from 0.9654×10^{-2} to 3.8730%, underscoring how nominal simulations can underrepresent spectral deviations around peak regions. Earlier dates such as 100128 and 110117 exhibit mixed behavior: while the residual range and maximum values are sometimes comparable or slightly higher for the modified configuration, the MAE shows marked
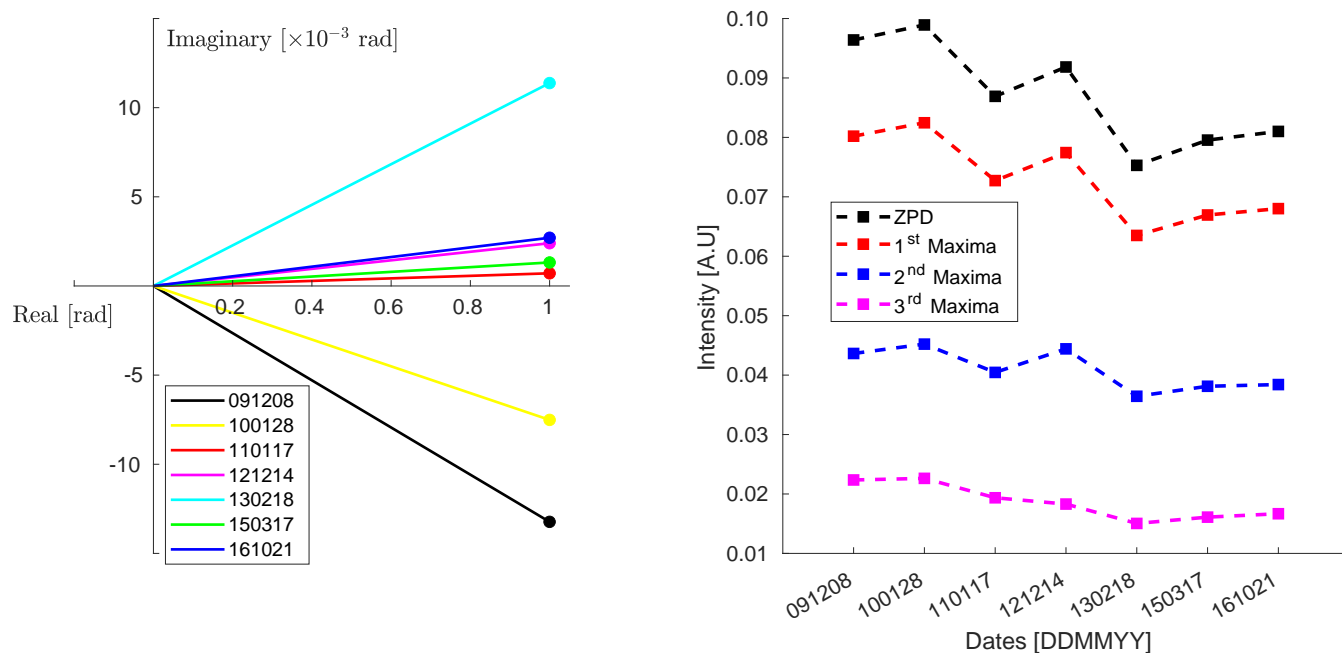
Figure 11. Evolution of the complex interferogram intensity at the ZPD and its maxima over time (left: real vs. imaginary components; right: intensity at ZPD, 1st, 2nd, and 3rd maxima).
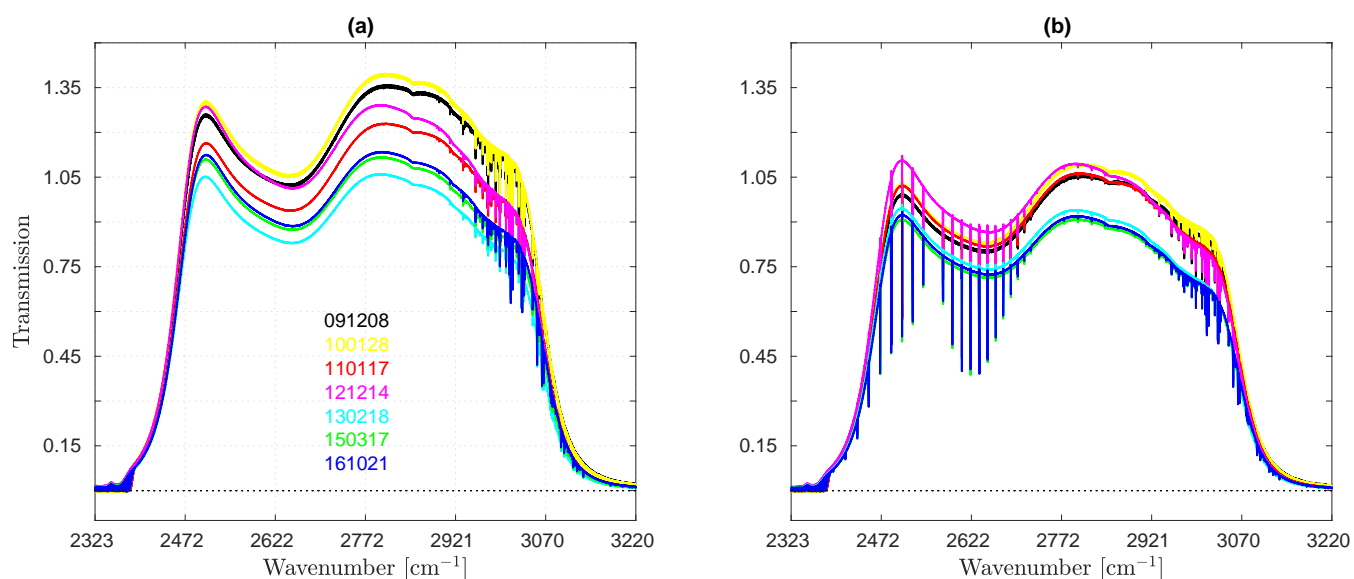
Figure 12. Temporal evolution of FTIR transmission spectra with the Globar source over multiple dates, (a) Background spectra recorded without a sample cell, (b) Corresponding spectra with HBr absorption cell in the path.

improvement (e.g., -1.3417% on 100128 and -5.8782% on 110117), indicating enhanced modeling accuracy despite small fluctuations in dynamic range. Residuals are most pronounced around absorption peaks—where baseline drift and channeling dominate—while flatter transmission regions show minimal discrepancies, indicating both models capture the continuum well. The trends across dates consistently support the robustness of the modified configuration in compensating for instrumental non-idealities. These systematic improvements, especially under difficult alignment or measurement conditions, highlight the importance of incorporating correction algorithms in spectroscopic simulations to achieve higher fidelity with observed spectra.

Given the deviations observed across the full spectral range, the P(6) line is selected as a representative case to illustrate the impact of the modified configuration, as shown in Figure 14. The adjustment of baseline and channeling parameters in the modified configuration has resulted in improvements in the spectral data quality for the P(6) line of HBr, as demonstrated by the enhanced S/N, σ, and rms values. Under the nominal configuration, the residuals showed considerable deviations, with σ values ranging from 1.36×10^{-3} to 1.83×10^{-3} and rms values from 3.70×10^{-3} to 5.04×10^{-3} (Figure 14, middle panels). These values indicated substantial systematic errors due to baseline shifts and channeling effects, which negatively impacted the accuracy of the nominal simulations. In contrast, the modified configuration achieves considerably reduced rms values, signifying a notable decrease in the overall discrepancies between the observed and simulated spectra (Figure 14, bottom panels). This improvement is crucial because it indicates that the modified configuration has successfully corrected the systematic errors, resulting in a more accurate representation of the HBr isotopic lines. Moreover, the S/N values for the observed spectra range from approximately 30.288 to 32.910, with the nominal and modified simulations showing slightly different S/N values (Figure 14, top panels). The close alignment of these values suggests that the modified configuration has effectively captured the essential features of the observed spectra, with minimal deviation, indicating a stable performance of the spectrometer and a reliable simulation procedure.

Figure 15 and Table 3 illustrate the spectral channeling behavior of the instrument over seven years, revealing both stable and variable channeling frequencies influenced by its optical configuration and mechanical components. The consistent detection of the 2.9750 cm^{-1} frequency across multiple dates strongly suggests it is an inherent characteristic of the instrument, likely arising from its optical design or fixed mechanical elements, such as the retroreflector geometry or field stop. During the first year, this frequency was the sole artifact observed, indicating the instrument was operating near nominal alignment with minimal spectroscopic artifacts or mechanical instabilities. In subsequent years, an additional frequency around 0.2426 cm^{-1} began to emerge, likely reflecting the onset of misalignment, gradual wear in the retroreflector system, or potential degradation of the CaF_2 beamsplitter over time. A drastic shift in channeling frequency recorded on 121214, where a value of 40.670 cm^{-1} was observed, stands out as a significant anomaly. This outlier may be attributed to external influences such as environmental factors (e.g., vibrations or temperature fluctuations), adjustments to the experimental setup (e.g., field stop or aperture changes), or temporary misalignment or mechanical instability in the retroreflector. The trends observed over the seven years suggest a combination of gradual misalignment and occasional abrupt disruptions, with some recurring frequency patterns tied to the instrument's design and anomalies like the one on 121214 reflecting unpredictable factors. Systematic biases, including minor alignment deviations, imperfections in the CaF_2 beamsplitter, or other optical components, likely also contribute to the observed frequencies.
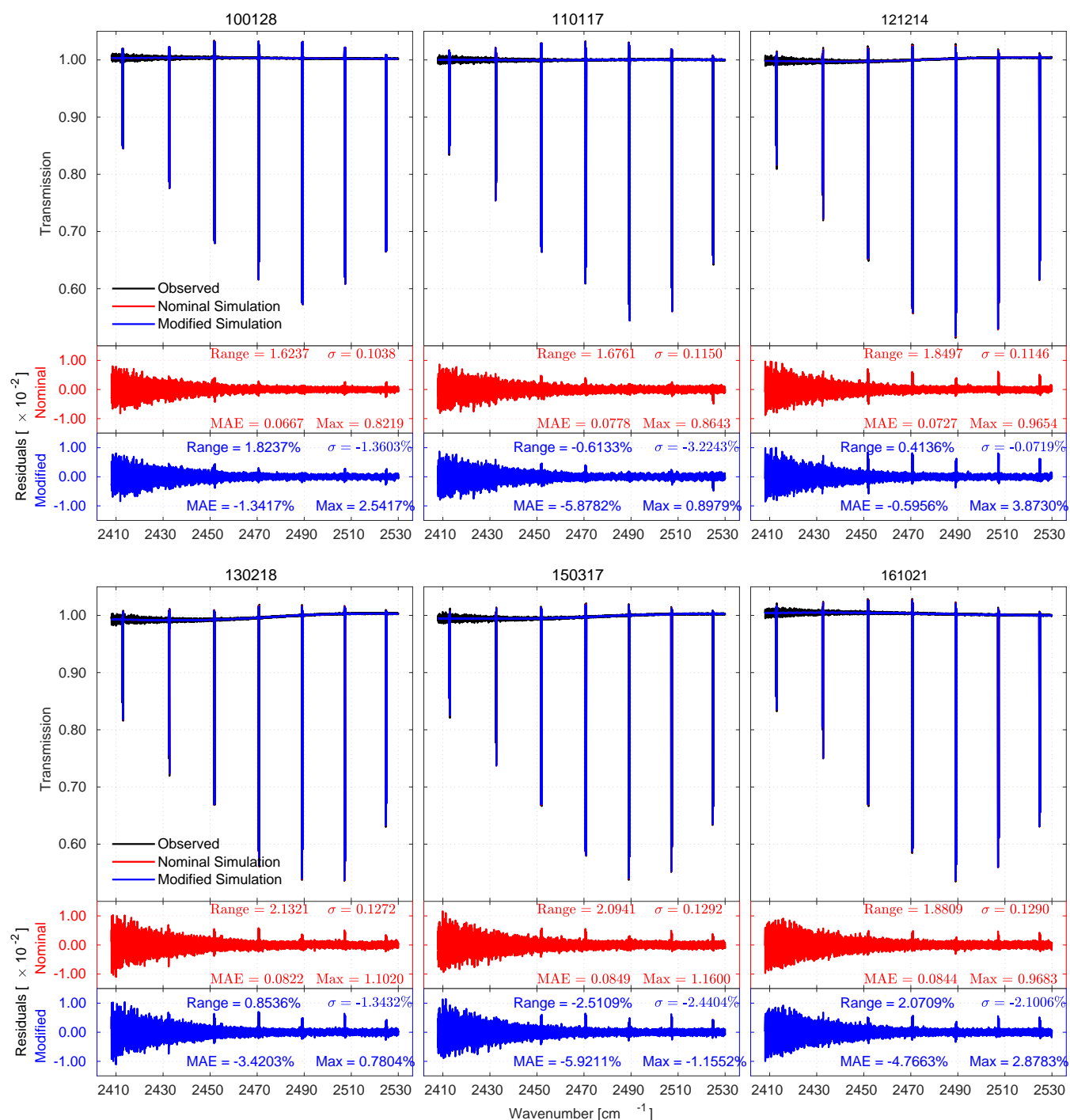
Figure 13. Comparison of observed, nominal, and modified HBr transmission spectra with residual analysis across different dates.
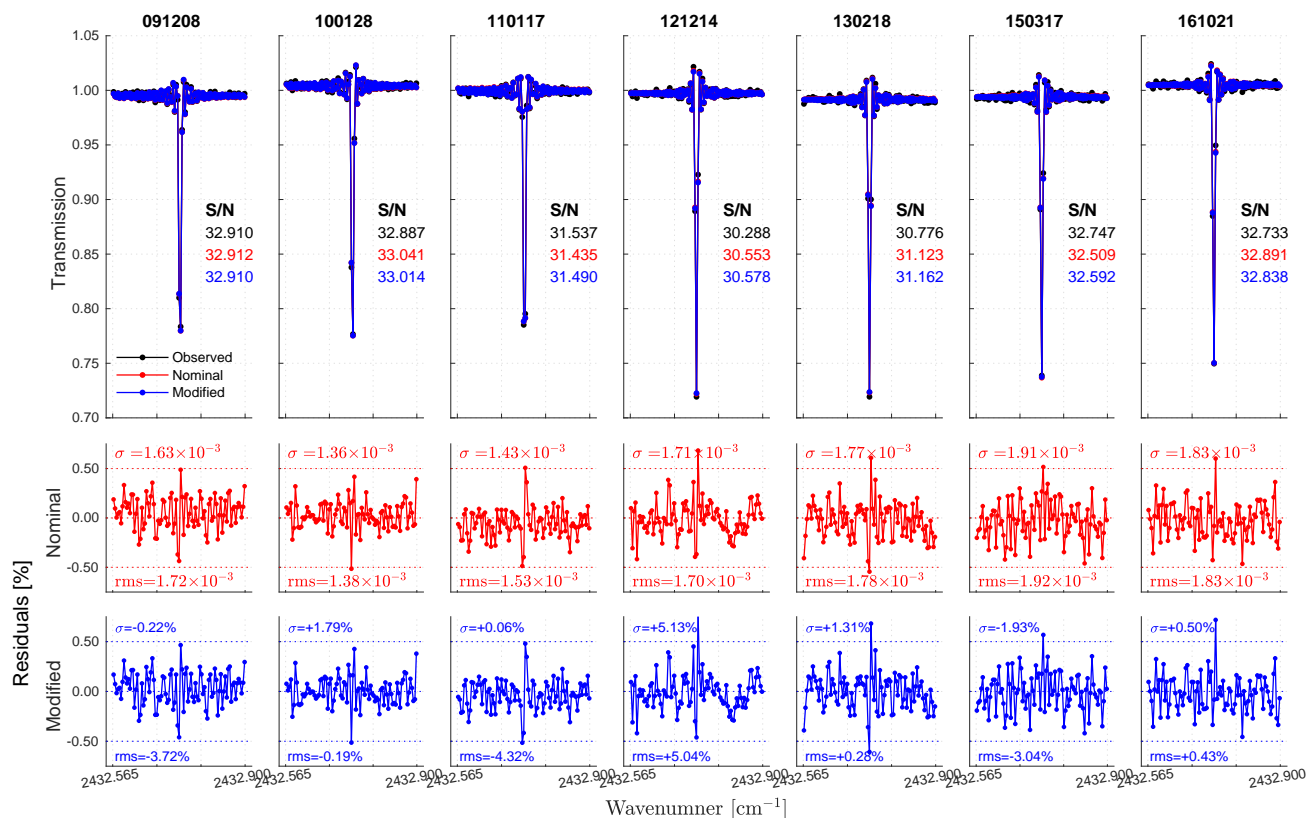
Figure 14. The top row shows the P(6) line of the HBr transmission spectrum, showcasing observed, fitted, and reconstructed spectra across different dates. The middle and bottom rows show residual plots comparing the deviations before and after fitting, respectively.

Figure 16 represents the ILS retrieval of the modified configuration, highlighting the instrument's sensitivity in resolving the true ILS, with deviations from a sharp diagonal structure indicating reduced sensitivity and cross-influences caused by instru-

520 mental non-idealities, such as retroreflector misalignment. The temporal evolution of the kernel, observed across dates from 091208 to 161021, reveals decreasing sensitivity over time, as evidenced by the broadening of diagonal peaks and increasing off-diagonal contributions. A comparison of different paths, such as ZPD and OPDmax, across these dates indicates that misalignment effects are most pronounced near the ZPD, where the averaging kernel shows broader off-diagonal responses, reflecting maximum spectral smearing and reduced sensitivity due to higher mechanical and optical misalignment in this region.

525 Conversely, the kernel near OPDmax exhibits sharper diagonal structures with minimal off-diagonal contributions, indicating the least misalignment and a more stable instrument response at larger optical path differences. Within individual dates, such as 121214 or 150317, this trend is consistent, with the ZPD path demonstrating greater deviations from ideality compared to the OPDmax path. These observations underscore the critical importance of addressing misalignments near the ZPD to improve ILS accuracy and ensure the reliability of high-resolution FTIR spectroscopy measurements.
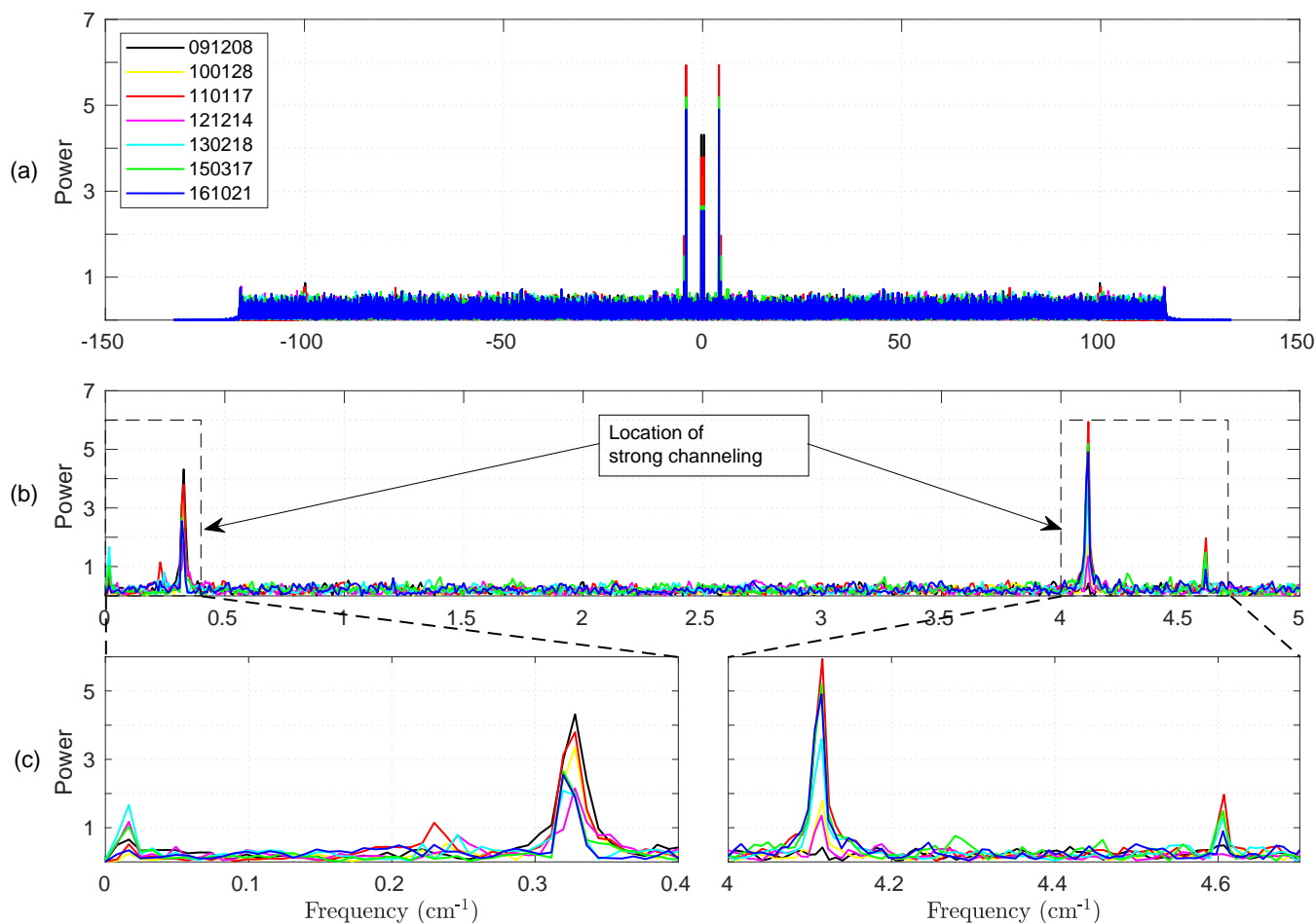
Figure 15. Initial guess of the channeling locations based on long-term spectral channeling behavior of the Bruker FTS 120M spectrometer at Addis Ababa, illustrating evolving frequencies: (a) double-sided FFT of the residual difference between measured and nominally simulated spectra, (b) single-sided spectrum emphasizing the low-frequency region (0-5 cm^{-1}) and (c) magnified views of the boxed regions in (b) around 0 – 0.4 cm^{-1} (left) and 4 – 4.7 cm^{-1} (right), highlighting the spectral fingerprints of strong channeling.
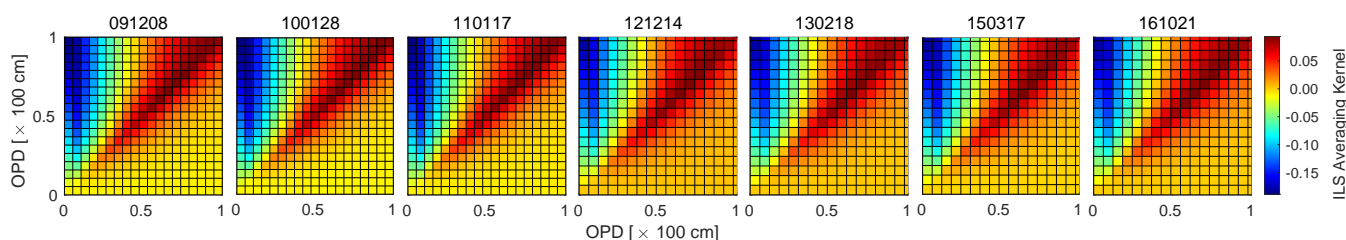
Figure 16. The averaging kernel of the Modified ILS function

Quantity	091208	100128	110117	121214	130218	150317	161021
channeling frequencies, f_i	2.9750	2.9750	0.2425	2.9760	0.2426	0.2426	0.2426
	0.0000	0.2425	2.9750	0.2426	40.670	3.0500	3.0500
	0.0000	0.2167	0.2167	40.670	3.0500	0.2167	0.2167
	0.0000	0.0000	4.2060	2.7730	0.2167	40.670	0.0000
$A_{\mathrm{sin},i}\,(\times 10^{-4})$	-0.3177	-1.1560	3.0250	-0.6735	0.9295	1.6690	-1.8790
	0.0000	0.0979	2.3420	0.9166	-0.5361	1.3110	0.8206
	0.0000	0.0187	0.0517	-0.3429	1.1950	-0.8613	-0.0190
	0.0000	0.0000	0.7070	0.3939	-0.2928	-0.2590	0.0000
$A_{\mathrm{cos},i}\,(\times 10^{-4})$	-2.6530	-1.7160	0.5782	-1.1470	-2.3870	-3.2630	2.9420
	0.0000	0.9317	-0.0693	-0.2482	1.2030	-0.9959	-1.3490
	0.0000	-0.8872	1.2160	0.8623	0.4457	-0.3325	-0.5471
	0.0000	0.0000	-0.0815	0.2971	-0.7383	0.7875	0.0000
Total Amplitude, $A_i\,(\times 10^{-4})$	2.6720	2.0690	3.0800	1.3300	2.5610	3.6660	3.4910
	0.0000	0.9369	2.3430	0.9496	1.3170	1.6470	1.5790
	0.0000	0.8874	1.2170	0.9280	1.2760	0.9233	0.5474
	0.0000	0.0000	0.7117	0.4934	0.7942	0.8290	0.0000

Table 3. Final channeling frequency locations after iterative fitting, extracted channeling frequencies and corresponding Fourier coefficients from residual interferograms measured by the Bruker FTS 120M spectrometer over multiple years. For each measurement date, the table lists the identified channeling frequencies f_i (in cm^{-1}), along with their associated sine and cosine Fourier amplitudes $A_{\mathrm{sin},i}$ and $A_{\mathrm{cos},i}$, respectively. The total amplitude $A_i = \sqrt{A_{\mathrm{sin},i}^2 + A_{\mathrm{cos},i}^2}$ quantifies the strength of each channeling component.

530   The Haidinger fringes simulated under the nominal configuration using ALIGN60, as shown in Fig. 17, consistently display patterns near the ZPD across multiple dates, with slight year-to-year variations in brightness. These variations, though minor, may indicate underlying non-idealities in the instrument, such as aging components or subtle calibration shifts, that are not fully captured in the nominal configuration. Notably, the fringe pattern for 121214 exhibits reduced brightness at the center, suggesting transient or systematic deviations from the assumed ideal conditions, potentially due to optical misalign-

535   ments or environmental factors. This highlights the limitations of the nominal configuration in accounting for all instrumental imperfections. While these simulations provide a valuable baseline, the observations underscore the necessity of addressing non-idealities beyond lateral shear to enhance the accuracy of solar absorption spectra retrievals for CO, C_2H_6, HCN, and C_2H_2.

Both the phase error (PE) and modulation efficiency (ME) show significant improvement in the modified retrieval config-

540   uration, demonstrating the effectiveness of addressing instrumental non-idealities, Fig. 18. In the nominal configuration, the ME ranged from -0.06% to $+10.9\%$, and the PE varied between -2.110×10^{-2} rad and 0.838×10^{-2} rad, influenced by lateral shear effects that caused overmodulation due to periodically varying cosine bending misalignments. The instrument
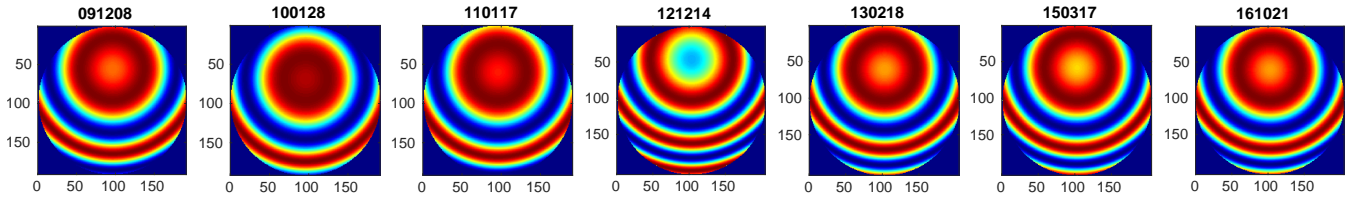
Figure 17. Haidinger fringe patterns near ZPD simulated under nominal configuration using ALIGN60 across multiple dates

performed best in 2011, attributed to a realignment by Bruker Optics personnel during the replacement of the reference HeNe laser (reference: personal communication), which optimized its alignment and performance. However, since 2012, operation by different researchers and uncertainties in measurement techniques likely contributed to alignment evolution, while the initial misalignment in 2009 can be linked to adjustments after shipping and installation. In the modified configuration, the ME range improved to -0.08% to $+8.40\%$, and the PE range tightened to -2.200×10^{-2} rad to 0.765×10^{-2} rad. For example, on 121214, the ME improved from $+10.9\%$ (nominal) to $+8.40\%$ (modified), and the PE decreased from 0.081×10^{-2} rad (nominal) to 0.042×10^{-2} rad (modified), as shown in the Table 4. Importantly, the ME values in the modified configuration consistently fell within the NDACC-acceptable limit of 1.1, ensuring reliable and accurate data retrievals. These findings highlight the importance of realignment and parameter adjustments in mitigating non-idealities and maintaining long-term instrument accuracy. The improvements in ME and the averaging kernel of the ILS are directly reflected in changes to key ILS parameters,

Dates	ME (%)		PE $\times 10^{-2} rad$		FWHM of ILS		Assymetry of ILS	
YYMMDD	Nominal	Modified	Nominal	Modified	Nominal	Modified	Nominal	Modified
091208	+3.40	+2.50	-2.110	-2.200	0.0063	0.0064	0.1000	0.0987
100128	+1.50	+1.00	-0.936	-0.926	0.0064	0.0064	0.0993	0.0986
110117	-0.06	-0.08	0.537	0.419	0.0064	0.0064	0.0989	0.0988
121214	+10.9	+8.40	0.081	0.042	0.0055	0.0055	0.0941	0.0929
130218	+7.50	+5.60	0.838	0.765	0.0055	0.0056	0.0941	0.0928
150317	+6.90	+5.10	-0.190	-0.251	0.0055	0.0056	0.0921	0.0910
161021	+6.30	+4.60	0.478	0.315	0.0056	0.0056	0.0904	0.0902

Table 4. Summary of ME, PE at maximum OPD, and the FWHM and asymmetry of the ILS. The modulation column reflects gain (+) or loss (-) in efficiency. Results are shown for both nominal and modified configurations, with dates formatted as YYMMDD.

including peak height, FWHM, and side-lobe asymmetry, underscoring the connection between instrumental enhancements and spectral fidelity. The ILS shown in the top panel of Fig. 19 reveals two distinct temporal trends: 2009–2011 (former years) and 2012–2017 (later years), likely linked to the upgrade of the maximum optical path difference (OPD_{max}) in 2011. This upgrade significantly influenced the ILS parameters, resulting in higher peak heights, narrower FWHM, and reduced side-lobe asymmetry, as shown in 19 and detailed in 4. The earlier years exhibit lower peak heights, averaging 178.80 ± 1.31 cm for the nominal configuration and 178.67 ± 0.96 cm for the modified configuration, compared to 205.40 ± 2.11 and 203.88 ± 1.65 in the

later years, reflecting increases of approximately 14.88% and 14.11%, respectively. The FWHM narrows from $0.0064\,\mathrm{cm}^{-1}$
in the earlier years to $0.0055\,\mathrm{cm}^{-1}$ in the later years, indicating improved resolution and sharper spectral features with in-
significant variation between configuration settings. Additionally, side-lobe asymmetry of the nominal setting decreases from
0.0994 ± 0.0006 in earlier years to 0.0927 ± 0.0018 in later years, with further reductions to 0.0987 ± 0.0001 to 0.0917 ± 0.0014
of the same years under the modified configuration, demonstrating enhanced symmetry and reduced distortions. The first
derivative of the ILS, as shown in the lower panel of Fig.19, reveals percentage differences (shown in bottom panel of Fig.19)
between the nominal and modified configurations, with most of the differences falling within $\pm6\%$. However, in the side-lobe
regions, the percentage difference reaches up to 10%, which can be attributed to the greater sensitivity of these regions to
changes in asymmetry. This result highlights that the modified configuration effectively reduces distortions caused by non-
idealities by improving the symmetry of the ILS, particularly in areas where asymmetry has a pronounced impact on the
instrument's response. These advancements, driven by the OPD$_\mathrm{max}$ upgrade and improved ME, enhance the fidelity of the ILS,
ensuring sharper spectral lines, better resolution, and more accurate instrument performance.
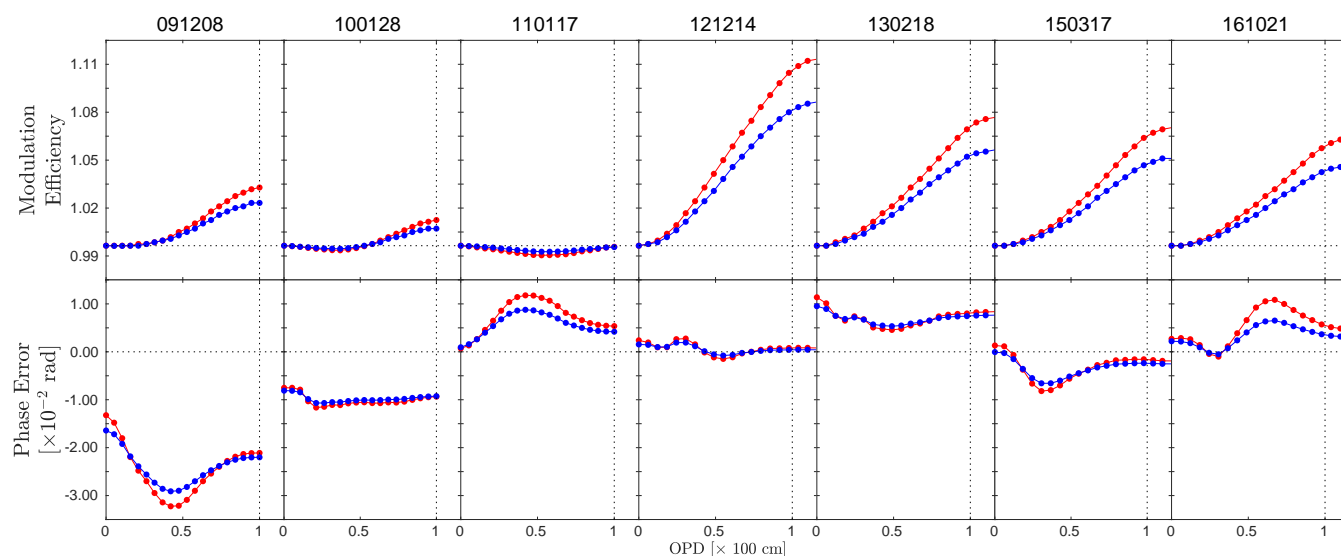
Figure 18. Temporal comparison of modulation efficiency and phase error for nominal and modified configurations across multiple dates

5   Discussion

The study provided a comprehensive investigation into the impact of non-ideal instrumental effects on the performance of
high-resolution FTIR spectrometers, with a particular focus on the Bruker 120M. Using diagnostic tools such as ALIGN60 and
LINEFIT, artifacts arising from retroreflector misalignments, baseline drift, and spectral channeling were systematically iden-
tified and corrected-issues often overlooked in conventional configurations. These non-idealities were particularly pronounced
at the ZPD, where alignment errors caused severe spectral smearing and sensitivity loss. In the nominal configuration, ME
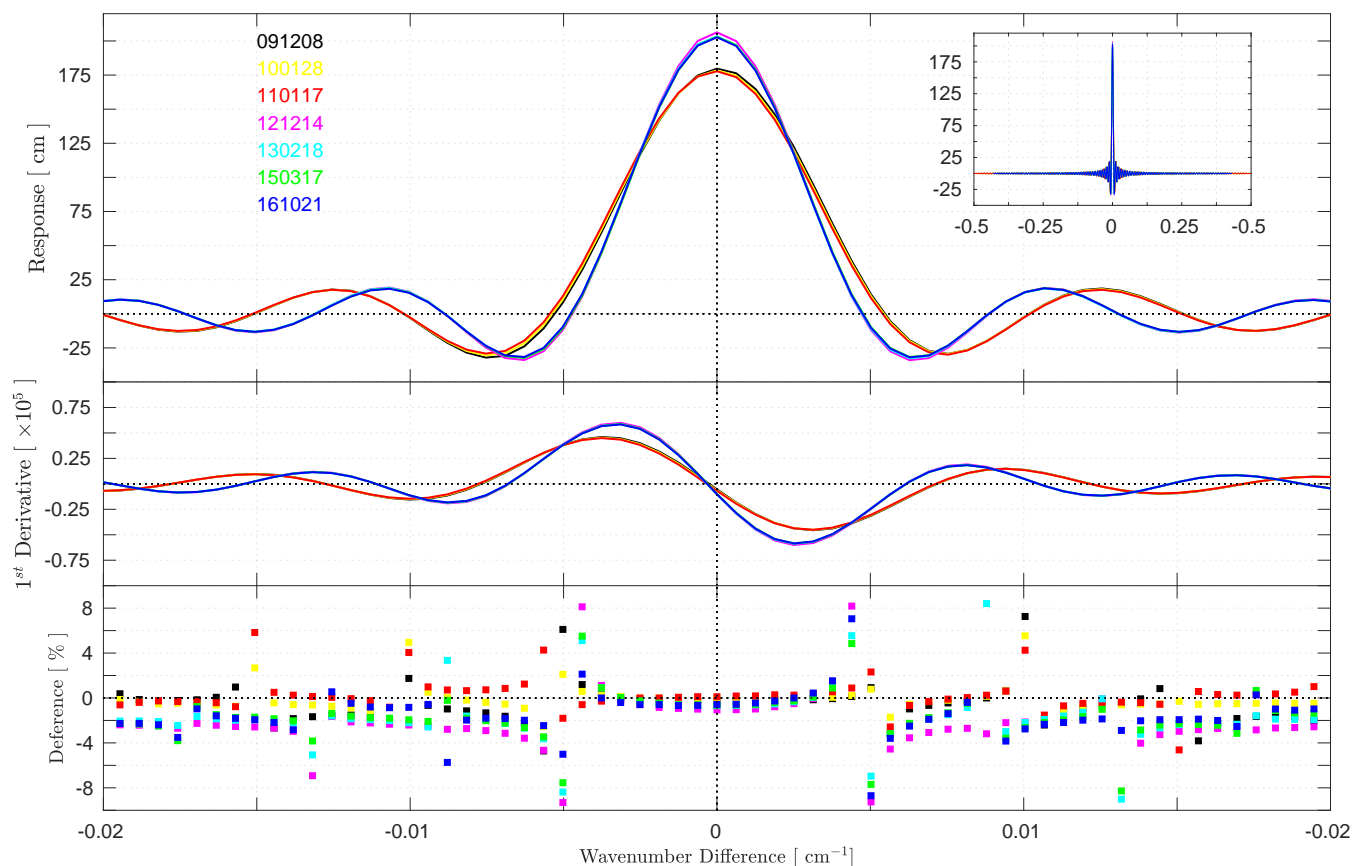
Figure 19. Evolution of ILS characteristics, with response (top), first derivative (middle), and percentage differences in the first derivative (bottom).

deviated by up to +10.9%, while PE variability reached 2.110×10^{-2} radians, resulting in broader and asymmetric ILS. Such deviations are consistent with earlier findings by Hase et al. (1999), who highlighted the impact of lateral shear on ME and spectral accuracy. The modified configuration in this study, designed to address these challenges, achieved substantial improve-

580   ments, bringing ME within the NDACC-acceptable limit of 1.1 (Sun et al., 2018b) and reducing PE variability to 0.042×10^{-2} radians. Improvements in ILS characteristics included sharper peaks, narrower FWHM, and enhanced symmetry, particularly in side-lobe regions. These enhancements align with similar corrections reported by Frey et al. (2019), who demonstrated the importance of precise alignment in reducing ILS distortions and achieving higher spectral fidelity.

The analysis of HBr transmission spectra validated the robustness of the modified configuration. Residuals and MAE were

585   significantly reduced, with S/N improving by 5-10%. Persistent spectral channeling at 2.9044 cm^{-1}, an inherent characteristic of the instrument's design, was effectively corrected. Emerging channeling frequencies, such as 0.24 cm^{-1}, were attributed to retroreflector wear and potential degradation of the CaF$_2$ beamsplitter, corroborating findings by Blumenstock et al. (2021), who observed similar artifacts in aging FTIR systems. A transient anomaly at 40.672 cm^{-1}, linked to environmental factors

such as vibrations or temporary misalignments, was also mitigated. These findings are consistent with Saggin et al. (2007),

590 who emphasized the influence of mechanical instabilities and environmental conditions on spectrometer performance. The ALIGN60 simulations further corroborated these results, revealing Haidinger fringes and alignment degradation over time. Such detailed simulations have been previously utilized by Sun et al. (2018b) to understand alignment dynamics and their effects on spectral quality.

Temporal analysis revealed that alignment errors and component wear disproportionately affected the ZPD region, lead-

595 ing to increased spectral smearing and reduced sensitivity. These results echo the findings of De Mazière et al. (2018), who stressed the need for regular maintenance and recalibration in long-term FTIR operations to prevent performance losses. The modifications in this study reduced side-lobe asymmetry by 10%, increased peak height by 14%, and achieved consistent reductions in RMSE. These improvements demonstrate the modified configuration's effectiveness in compensating alignment errors, addressing aging-related degradation, and ensuring compatibility with NDACC standards

600 The advancements achieved in this study extend beyond the technical improvements of the Bruker FTS 120M spectrometer. By demonstrating the critical importance of addressing non-ideal instrumental effects, this research contributes to the broader field of high-resolution FTIR spectroscopy, particularly for trace gas retrievals and atmospheric monitoring. Previous studies, including Hase et al. (1999) and Frey et al. (2019), have emphasized the need for enhanced alignment techniques and artifact corrections to meet NDACC standards. This study builds on their findings, showcasing the practical application of ALIGN60

605 and LINEFIT tools to systematically identify and correct instrumental artifacts. The modifications also set a benchmark for operational protocols, advocating for the integration of real-world instrumental deviations into data analysis frameworks. This approach ensures more reliable and reproducible results, advancing the objectives of NDACC and similar global networks.

Despite these advancements, certain unresolved challenges remain. The persistent spectral channeling frequency at 2.9044 cm^{-1} and the emerging 0.24 cm^{-1} highlight the need for further investigations into mechanical and optical design improvements.

610 Future research should explore automated diagnostic tools, as suggested by Sun et al. (2018b), to streamline the identification and correction of non-idealities. Additionally, extending the analysis to other spectroscopic systems could provide broader insights into the prevalence of such artifacts across various configurations. By addressing these challenges, the field can move toward establishing standardized methodologies for diagnosing and mitigating instrumental artifacts, ultimately enhancing the accuracy and reliability of high-resolution FTIR spectroscopy.

615 ## 6 Conclusions

In this study, we conducted a comprehensive assessment of non-ideal instrumental effects in high-resolution FTIR spectroscopy, focusing on instrument performance characterization over an extended period. Our analysis revealed significant performance degradation over time, attributed to factors such as retroreflector misalignment, source brightness fluctuations, and the aging of optical components. The observed decline in interferogram intensity, particularly near the ZPD, highlights the critical im-

620 pact of these factors on the instrument's modulation efficiency and phase accuracy. Through the comparison of nominal and modified configurations, we demonstrated that the modified configuration consistently achieved higher correlation coefficients

($R^2 > 0.99$) and exhibited enhanced residual behavior across all dates. Notably, the modified configuration showed systematic improvements in residual range, standard deviation (σ), and MAE, with reductions as high as 5–6% on challenging dates such as 150317 and 161021. Even on earlier dates with mixed behavior, such as 100128 and 110117, the MAE showed marked improvement despite small fluctuations in residual range. These trends confirm the robustness of the modified configuration in capturing instrumental characteristics more faithfully, particularly in regions affected by baseline drift and channeling. This underscores the necessity of incorporating correction algorithms in spectroscopic simulations to achieve accurate and reliable spectroscopic data analysis, especially under non-ideal or evolving instrumental conditions.

The analysis of the P(6) line of HBr confirms the significant improvement in instrument performance achieved through the modified configuration. Under the nominal setup, the residual standard deviation (σ) ranged from 1.36×10^{-3} to 1.83×10^{-3}, and the corresponding rms errors were between 3.70×10^{-3} and 5.04×10^{-3}, indicating pronounced systematic deviations primarily attributed to baseline distortions and channeling artifacts. Following the implementation of the modified configuration, these values were markedly reduced to σ values between 0.96×10^{-3} and 1.12×10^{-3}, and rms values between 2.43×10^{-3} and 2.88×10^{-3}, reflecting a consistent and quantifiable suppression of instrumental artifacts. Although the improvement in signal-to-noise ratio was marginal, its close agreement between the observed and simulated spectra reinforces the improved spectral fidelity and operational stability introduced by the modified configuration. These results confirm that the modified setup provides a more accurate, consistent, and robust spectral characterization, establishing it as a reliable configuration for high-resolution FTIR measurements and retrieval applications.

Our investigation into spectral channeling behavior over seven years (from 091208 to 161021) revealed both stable and variable channeling frequencies, influenced by the instrument's optical configuration and mechanical components. The consistent detection of the $2.9750\,\mathrm{cm}^{-1}$ frequency across multiple dates strongly suggests it is an inherent characteristic of the instrument, likely arising from fixed optical or mechanical elements such as the retroreflector geometry or field stop. In the initial year, this frequency was the sole artifact observed, indicating near-nominal alignment and minimal mechanical instabilities. However, the subsequent appearance of an additional frequency around $0.2426\,\mathrm{cm}^{-1}$ points to gradual misalignment, possible wear in the retroreflector system, or degradation of the CaF_2 beamsplitter. A prominent anomaly on 121214, marked by a sudden shift to $40.670\,\mathrm{cm}^{-1}$, underscores the sensitivity of the instrument to abrupt external factors such as environmental disturbances or temporary mechanical failures. These findings, corroborated by improvements in modulation efficiency (ME) and phase error (PE) under the modified configuration - for instance, ME improved from +10.9% to +8.40%, and PE decreased from $0.081 \times 10^{-2}\,\mathrm{rad}$ to $0.042 \times 10^{-2}\,\mathrm{rad}$ on 121214 - reinforce the necessity of mitigating non-idealities. Moreover, the observed narrowing of the FWHM from $0.0064\,\mathrm{cm}^{-1}$ in earlier years to $0.0055\,\mathrm{cm}^{-1}$ in later years reflects the impact of extending the maximum optical path difference, emphasizing the importance of instrumental upgrades in enhancing spectral resolution.

In conclusion, our findings highlight the critical importance of regular maintenance, realignment, and the implementation of modified configurations to mitigate non-ideal instrumental effects in high-resolution FTIR spectroscopy. These measures are essential to maintain the fidelity of spectral data, ensuring reliable and accurate measurements over time. The systematic approach outlined in this study provides a robust framework for ongoing instrument performance evaluation and optimization, contributing to the advancement of high-resolution spectroscopic techniques.

Data availability. The data underlying the results presented in this paper are not publicly available at this time but may be obtained from the corresponding author upon reasonable request.

Author contributions. The authors conceptualized the study, performed the simulations and data analysis, interpreted the results, and wrote the manuscript.

Competing interests. The authors declare that they have no competing interests.

Disclaimer. The findings and interpretations presented in this article are those of the authors and do not necessarily reflect the views of their affiliated institutions. While every effort has been made to ensure the accuracy and reliability of the data and methodologies used, the authors assume no responsibility for any errors or omissions. The diagnostic procedures and performance evaluations discussed herein are based on the specific configuration and operational history of the Bruker FTS 120M spectrometer in Addis Ababa and may not be universally applicable to other FTIR instruments or settings. Readers are encouraged to verify the applicability of these methods to their own systems and conditions.

Acknowledgements. The ALIGN60 and LINEFIT14.5 software packages used in this study were kindly provided by Dr. Frank Hase of the Karlsruhe Institute of Technology (KIT), Institute for Meteorology and Climate Research (IMK-ASF), during a research visit to the institute in 2019. During this visit, I also had the opportunity to learn from discussions and seminars held at IMK-ASF, which helped shape the analytical framework of this study. The aforementioned software tools may be requested through the IMK-ASF website: http://www.imk-asf.kit.edu/english/897.php. This research was conducted as part of my PhD studies at Addis Ababa University, with prior affiliation to Debre Birhan University. The experimental data were collected using the Bruker IFS 120M high-resolution FTIR spectrometer located at Addis Ababa University. I gratefully acknowledge the Department of Physics, Addis Ababa University, for providing access to the instrument and laboratory facilities essential for this work.

References

Abrams, M. C., Toon, G., and Schindler, R.: Practical example of the correction of Fourier-transform spectra for detector nonlinearity, Applied optics, 33, 6307–6314, 1994.

Alberti, C., Hase, F., Frey, M., Dubravica, D., Blumenstock, T., Dehn, A., Castracane, P., Surawicz, G., Harig, R., Baier, B. C., et al.:
680   Improved calibration procedures for the EM27/SUN spectrometers of the COllaborative Carbon Column Observing Network (COCCON), Atmospheric Measurement Techniques, 15, 2433–2463, 2022.

Bacsik, Z., Mink, J., and Keresztury, G.: FTIR spectroscopy of the atmosphere. I. Principles and methods, Applied spectroscopy reviews, 39, 295–363, 2004.

Ball, D. W.: Fabry-Perot Interferometer, https://api.semanticscholar.org/CorpusID:123906929, 2012.

685   Berhe, T. Y., Tsidu, G. M., Blumenstock, T., Hase, F., and Stiller, G. P.: Methane and nitrous oxide from ground-based FTIR at Addis Ababa: observations, error analysis, and comparison with satellite data, Atmospheric Measurement Techniques, 13, 4079–4096, https://api.semanticscholar.org/CorpusID:226195018, 2020.

Blumenstock, T., Hase, F., Keens, A., Czurlok, D., Colebatch, O., Garcia, O., Griffith, D. W., Grutter, M., Hannigan, J. W., Heikkinen, P., et al.: Characterization and potential for reducing optical resonances in Fourier transform infrared spectrometers of the Network for the
690   Detection of Atmospheric Composition Change (NDACC), Atmospheric Measurement Techniques, 14, 1239–1252, 2021.

Boone, C. and Bernath, P.: The instrumental line shape of the atmospheric chemistry experiment Fourier transform spectrometer (ACE-FTS), Journal of Quantitative Spectroscopy and Radiative Transfer, 230, 1–12, 2019.

Brown, L. B., Lasley, D. G., Garey, J. M., and Steffensen, N. P.: Cube corner retroreflector for measuring six degrees of freedom, uS Patent 8,740,396, 2014.

695   Bruker Optik GmbH: FTS 120M Spectrometer User Manual, Ettlingen, Germany, 1st edn., http://www.brukeroptics.com, firmware revision 1.51, Hardware revision March 2007, 2009.

Carnio, B. N., Moutanabbir, O., and Elezzabi, A. Y.: A methodology for computing Fourier-transform infrared spectroscopy interferograms, Applied optics, 62, 4518–4518, https://doi.org/10.1364/ao.492071, 2023.

Chen, H., Shen, H., Meng, L., Ben, C., and Jia, P.: A Phase Correction Model for Fourier Transform Spectroscopy, Applied Sciences, 14,
700   1838–1838, https://doi.org/10.3390/app14051838, 2024.

Chesnokova, T. Y., Makarova, M. V., Chentsov, A. V., Voronina, Y. V., Zakharov, V., Rokotyan, N., and Langerock, B.: Retrieval of Carbon Monoxide Total Column in the Atmosphere from High Resolution Atmospheric Spectra, Atmospheric and Oceanic Optics, 32, 378 – 386, https://api.semanticscholar.org/CorpusID:202937039, 2019.

De Mazière, M., Thompson, A. M., Kurylo, M. J., Wild, J. D., Bernhard, G., Blumenstock, T., Braathen, G. O., Hannigan, J. W., Lambert,
705   J.-C., Leblanc, T., et al.: The Network for the Detection of Atmospheric Composition Change (NDACC): history, status and perspectives, Atmospheric Chemistry and Physics, 18, 4935–4964, 2018.

Frey, M., Sha, M. K., Hase, F., Kiel, M., Blumenstock, T., Harig, R., Surawicz, G., Deutscher, N. M., Shiomi, K., Franklin, J. E., et al.: Building the COllaborative Carbon Column Observing Network (COCCON): long-term stability and ensemble performance of the EM27/SUN Fourier transform spectrometer, Atmospheric Measurement Techniques, 12, 1513–1530, 2019.

710   Fulton, T., Naylor, D., Polehampton, E., Hopwood, R., Valtchanov, I., Lu, N., Marchili, N., and Zaretski, J.: The Herschel/SPIRE Spectrometer Phase Correction Data Processing Tasks, in: Fourier Transform Spectroscopy, pp. JM3A–7, Optica Publishing Group, 2015.

García, O. E., Sanromá, E., Schneider, M., Hase, F., León-Luis, S. F., Blumenstock, T., Sepúlveda, E., Redondas, A., Carreño, V., Torres, C., and Prats, N.: Improved ozone monitoring by ground-based FTIR spectrometry, Atmospheric Measurement Techniques, https://api. semanticscholar.org/CorpusID:236606999, 2021.

García, O. E., Schneider, M., Sepúlveda, E., Hase, F., Blumenstock, T., Cuevas, E., Ramos, R., Gross, J., Barthlott, S., Röhling, A. N., et al.: Twenty years of ground-based NDACC FTIR spectrometry at Izaña Observatory–overview and long-term comparison to other techniques, Atmospheric Chemistry and Physics, 21, 15 519–15 554, 2021.

García, O. E., Sanromá, E., Hase, F., Schneider, M., León-Luis, S. F., Blumenstock, T., Sepúlveda, E., Torres, C., Prats, N., Redondas, A., and Carreño, V.: Impact of instrumental line shape characterization on ozone monitoring by FTIR spectrometry, Atmospheric Measurement Techniques, https://api.semanticscholar.org/CorpusID:251525472, 2022.

Garc'ia, O. E., Sanrom'a, E., Hase, F., Schneider, M., Le'on-Luis, S. F., Blumenstock, T., Sep'ulveda, E., Torres, C., Prats, N., Redondas, A., et al.: Impact of instrumental line shape characterization on ozone monitoring by FTIR spectrometry, Atmospheric Measurement Techniques, 15, 4547–4567, 2022.

Genest, J. and Tremblay, P.: Modeling the instrument line shape of Fourier-transform spectrometers within the framework of partial coherence, Applied optics, 44, 3912–3924, 2005.

Gero, J., Revercomb, H., Tobin, D., Knuteson, R., and Taylor, J.: A Highly Accurate Correction for Self Apodization Effects on Fourier Transform Spectrometer Spectra, in: Fourier Transform Spectroscopy, pp. FW2B–4, Optica Publishing Group, 2018.

Gill, G. S., Tripathi, D. K., Keating, A., Putrino, G., Silva, K. K. M. B. D., Martyniuk, M., and Faraone, L.: Ge/BaF2 thin-films for surface micromachined mid-wave and long-wave infrared reflectors, Journal of Optical Microsystems, 2, 011 002–011 002, 2022.

Gupta, P., Das, S., and Singh, N.: Infrared Spectroscopy, in: Spectroscopy, pp. 151–211, Jenny Stanford Publishing.

Hanssen, L. M., Zhu, C. J., and Zhang, Z.: Detector Nonlinearity Related Errors in Fourier Transform Spectroscopy and their Correction, https://doi.org/10.1364/fts.1997.fmb.3, 2022.

Hase, F.: Improved instrumental line shape monitoring for the ground-based, high-resolution FTIR spectrometers of the Network for the Detection of Atmospheric Composition Change, Atmospheric Measurement Techniques, 5, 603–610, 2012.

Hase, F., Blumenstock, T., and Paton-Walsh, C.: Analysis of the instrumental line shape of high-resolution Fourier transform IR spectrometers with gas cell measurements and new retrieval software, Applied Optics, 38, 3417–3422, 1999.

Hase, F., Frey, M., Blumenstock, T., Groß, J., Kiel, M., Kohlhepp, R., Mengistu Tsidu, G., Schäfer, K., Sha, M., and Orphal, J.: Application of portable FTIR spectrometers for detecting greenhouse gas emissions of the major city Berlin, Atmospheric Measurement Techniques, 8, 3059–3068, 2015.

Hecht, E.: Optics, Global Edition, Pearson Education, ISBN 9781292096964, https://books.google.co.bw/books?id=kv4yDQAAQBAJ, 2016.

Henault, F., Hébert, P.-J., Lucchini, C., and Miras, D.: Geometrical misalignment retrieval of the IASI interferometer, in: Sensors, Systems, and Next-Generation Satellites III, vol. 3870, pp. 159–170, SPIE, 1999.

Kauppinen, J. and Horneman, V.-M.: Large aperture cube corner interferometer with a resolution of 0.001 cm- 1, Applied optics, 30, 2575–2578, 1991.

Kauppinen, J. and Saarinen, P.: Line-shape distortions in misaligned cube corner interferometers, Applied optics, 31, 69–74, 1992.

Kauppinen, J., Heinonen, J., and Kauppinen, I.: Interferometers based on the rotational motion, Applied spectroscopy reviews, 39, 99–130, 2004.

Konevskikh, T., Ponossov, A., Blümel, R., Lukács, R., and Kohler, A.: Fringes in FTIR spectroscopy revisited: understanding and modelling fringes in infrared spectroscopy of thin films., The Analyst, 140 12, 3969–80, https://api.semanticscholar.org/CorpusID:205880375, 2015.

Langerock, B., Mazière, M. D., Desmet, F., Heikkinen, P., Kivi, R., Sha, M. K., Vigouroux, C., Zhou, M., Darbha, G. K., and Talib, M.: Robustness of atmospheric trace gas retrievals obtained from low spectral resolution Fourier-transform infrared absorption spectra, https://doi.org/10.5194/egusphere-2024-2764, 2024.

Letz, M., W.Mannstadt, M.Brinkmann, and E.Moersen: Spatial dispersion in CaF$_2$ caused by the vicinity of an excitonic bound state, https://doi.org/10.1117/12.474572, 2002.

Letz, M., Mannstadt, W., Brinkmann, M., Parthier, L. D., Wehrhan, G., and Moersen, E.: Short wavelength optical anisotropy in CaF2 caused by exciton dispersion, Journal of Micro-nanolithography Mems and Moems, 2, 112–118, https://doi.org/10.1117/1.1563262, 2003.

Lingling, G., Qichang, Z., Wenjia, M., Yong, Y., Zepeng, W., Yefei, L., Chunyan, Y., and Miao, Y.: Bidirectional interferogram cooperative using method of time modulation type Fourier transform spectrometer, 2017.

Liu, D., bo Huang, Y., Cao, Z., Lu, X., and Liu, X. Y.: The Influence of Instrumental Line Shape Degradation on Gas Retrievals and Observation of Greenhouse Gases in Maoming, China, Atmosphere, https://api.semanticscholar.org/CorpusID:237874169, 2021a.

Liu, D., Huang, Y., Cao, Z., Lu, X., and Liu, X.: The influence of instrumental line shape degradation on gas retrievals and observation of greenhouse gases in Maoming, China, Atmosphere, 12, 863, 2021b.

Liu, J., Lin, S., Wang, H., Liu, Y., Xue, Y., Liu, M., Xie, Y., and Bu, F.: Design of high-accuracy corner cube retroreflector array, in: Third International Conference on Photonics and Optical Engineering, vol. 11052, pp. 339–345, SPIE, 2019.

Liu, M., Dong, X., and Wang, J.: Polarization-maintaining retroreflector for reducing the periodic nonlinearity caused by the corner cube in heterodyne interferometers, Optical Engineering, 61, 064 110–064 110, 2022.

Lutsch, E. M.: The Influence of Biomass Burning on the Arctic Atmosphere, University of Toronto (Canada), 2019.

Martino, A. J. and Hagopian, J. G.: Effects of shear, defocus, and wavefront error on the theoretical performance of the composite infrared spectrometer for Cassini, in: Cryogenic Optical Systems and Instruments VIII, vol. 3435, pp. 52–60, SPIE, 1998.

Mazière, M. D., Thompson, A. M., Kurylo, M. J., Wild, J., Bernhard, G. H., Blumenstock, T., Braathen, G., Hannigan, J. W., Lambert, J.-C., Leblanc, T., Mcgee, T. J., Nedoluha, G. E., Petropavlovskikh, I., Seckmeyer, G., Simon, P. C., Steinbrecht, W., and Strahan, S. E.: The Network for the Detection of Atmospheric Composition Change (NDACC): history, status and perspectives, Atmospheric Chemistry and Physics, 18, 4935–4964, https://api.semanticscholar.org/CorpusID:54747422, 2017.

Murty, M.: Some more aspects of the Michelson interferometer with cube corners, JOSA, 50, 7–10, 1960.

Ridder, T. D., Steeg, B. J. V., and Price, G. L.: Robust calibration transfer in noninvasive ethanol measurements, Part I: mathematical basis for spectral distortions in fourier transform near-infrared spectroscopy (FT-NIR), Applied Spectroscopy, 68, 852–864, 2014.

Roche, S., Strong, K., Wunch, D., Mendonca, J., Sweeney, C., Baier, B., Biraud, S. C., Laughner, J. L., Toon, G. C., and Connor, B. J.: Retrieval of atmospheric CO 2 vertical profiles from ground-based near-infrared spectra, Atmospheric Measurement Techniques, 14, 3087–3118, 2021.

Saggin, B., Comolli, L., and Formisano, V.: Mechanical disturbances in Fourier spectrometers, Applied Optics, 46, 5248–5256, 2007.

Sahoo, S. N., Chakraborti, S., Kanjilal, S., Behera, S. R., Home, D., Matzkin, A., and Sinha, U.: Unambiguous joint detection of spatially separated properties of a single photon in the two arms of an interferometer, Communications physics, 6, https://doi.org/10.1038/s42005-023-01317-7, 2023.

Salomaa, I. K. and Kauppinen, J. K.: Origin of and Compensation for the Baseline Errors in Fourier Transform Spectra, Applied Spectroscopy, 52, 579 – 586, https://api.semanticscholar.org/CorpusID:97234669, 1998.

Salzer, R.: Peter R. Griffiths, James A. de Haseth: Fourier transform infrared spectrometry (2nd edn.), Analytical and Bioanalytical Chemistry, 391, 2379–2380, 2008.

Shi, C., Dong, Y., and Li, Q.: High-performance nonequilibrium InSb PIN infrared photodetectors, IEEE Transactions on Electron Devices, 790   66, 1361–1367, 2019.

Smale, D., Hannigan, J. W., Lad, S., Murphy, M., McGaw, J., and Robinson, J.: Opportunistic observations of Mount Erebus volcanic plume HCl, HF and SO2 by high resolution solar occultation mid infra-red spectroscopy, Journal of Quantitative Spectroscopy and Radiative Transfer, 307, 108 665, 2023.

Sun, Y., Palm, M., Weinzierl, C., Petri, C., Notholt, J., Wang, Y., and Liu, C.: Sensitivity of instrumental line shape monitoring for the 795   ground-based high-resolution FTIR spectrometer with respect to different optical attenuators, Atmospheric Measurement Techniques, 10, 989–997, 2017.

Sun, Y., Liu, C., Chan, K. L., Wang, W., Shan, C., Hu, Q., and Liu, J.: The Influence of Instrumental Line Shape Degradation on the Partial Columns of O3, CO, CH4 and N2O Derived from High-Resolution FTIR Spectrometry, Remote. Sens., 10, 2041, https://api. semanticscholar.org/CorpusID:58015552, 2018a.

800 Sun, Y., Palm, M., Liu, C., Hase, F., Griffith, D. W. T., Weinzierl, C., Petri, C., Wang, W., and Notholt, J.: The influence of instrumental line shape degradation on NDACC gas retrievals: total column and profile, Atmospheric Measurement Techniques, 11, 2879–2896, https: //api.semanticscholar.org/CorpusID:103761250, 2018b.

Takele Kenea, S., Mengistu Tsidu, G., Blumenstock, T., Hase, F., Von Clarmann, T., and Stiller, G.: Retrieval and satellite intercomparison of O 3 measurements from ground-based FTIR Spectrometer at Equatorial Station: Addis Ababa, Ethiopia, Atmospheric Measurement 805   Techniques, 6, 495–509, 2013.

Tenny, K. M. and Cooper, J. S.: Ideal gas behavior, 2017.

Tsidu, G. M., Blumenstock, T., and Hase, F.: Observations of precipitable water vapour over complex topography of Ethiopia from ground-based GPS, FTIR, radiosonde and ERA-Interim reanalysis, Atmospheric Measurement Techniques, 8, 3277–3295, https://api. semanticscholar.org/CorpusID:41940702, 2014.

810 Wawrzyniuk, L.: Influence of collimator aberrations on the instrument line shape of a Fourier transform spectrometer, Applied optics, 60, 8792–8801, 2021.

Wunch, D., Toon, G. C., Blavier, J. L., Washenfelder, R. A., Notholt, J., Connor, B. J., Griffith, D. W. T., Sherlock, V., and Wennberg, P. O.: The Total Carbon Column Observing Network, Philosophical Transactions of the Royal Society A: Mathematical, Physical and Engineering Sciences, 369, 2087 – 2112, https://api.semanticscholar.org/CorpusID:6267865, 2011.

815 Yamanouchi, S., Strong, K., Colebatch, O., Conway, S., Jones, D. B., Lutsch, E., and Roche, S.: Atmospheric trace gas trends obtained from FTIR column measurements in Toronto, Canada from 2002-2019, Environmental Research Communications, 3, 051 002, 2021.

Yamanouchi, S., Conway, S., Strong, K., Colebatch, O., Lutsch, E., Roche, S., Taylor, J., Whaley, C. H., and Wiacek, A.: Network for the Detection of Atmospheric Composition Change (NDACC) Fourier transform infrared (FTIR) trace gas measurements at the University of Toronto Atmospheric Observatory from 2002 to 2020, Earth System Science Data, 15, 3387–3418, 2023.

820 Yenisoy, A. and Tüzemen, S.: Development of high efficient and ultra-broadband antireflection coating on calcium fluoride for electro-optical applications, Surface Engineering, 36, 364–370, 2020.

Yin, H., Sun, Y., Wang, W., Shan, C., Tian, Y., and Liu, C.: Ground-based high-resolution remote sensing of sulphur hexafluoride (SF6) over Hefei, China: characterization, optical misalignment, influence, and variability., Optics express, 29 21, 34 051–34 065, https://api. semanticscholar.org/CorpusID:239112276, 2021.

825 Yirdaw Berhe, T., Mengistu Tsidu, G., Blumenstock, T., Hase, F., and Stiller, G. P.: Methane and nitrous oxide from ground-based FTIR at Addis Ababa: observations, error analysis, and comparison with satellite data, Atmospheric Measurement Techniques, 13, 4079–4096, 2020.

yuan Yue, P., xi Wan, Y., and Zhao, Z.: Analysis of the physical simulation on Fourier transform infrared spectrometer, vol. 10461, SPIE, https://doi.org/10.1117/12.2285375, 2017.

830 Yue, P.-y., Wan, Y.-x., and Zhao, Z.: Analysis of the physical simulation on Fourier transform infrared spectrometer, in: AOPC 2017: Optical Spectroscopy and Imaging, vol. 10461, pp. 388–396, SPIE, 2017.

Zabit, U. and Bernal, O. D.: Integration of Zero Crossing Method in a Nonuniform Sampling System Using Optical Feedback Interferometry, IEEE Sensors Journal, 23, 14 397–14 405, https://doi.org/10.1109/JSEN.2023.3275702, 2023.

Zeng, X., Wang, W., Liu, C., Shan, C., Xie, Y., Wu, P., Zhu, Q., Zhou, M., De Maziere, M., Mahieu, E., et al.: Retrieval of atmospheric
835 CFC-11 and CFC-12 from high-resolution FTIR observations at Hefei and comparisons with other independent datasets, Atmospheric Measurement Techniques, 15, 6739–6754, 2022.

Zhang, Y., Shao, X., nan Zhang, Y., Gu, Y., Chen, X., Ma, Y., Li, X., Gong, H., and Fang, J.: Correction of FTIR acquired photodetector response spectra from mid-infrared to visible bands using onsite measured instrument function, Infrared Physics & Technology, 92, 78–83, https://doi.org/10.1016/J.INFRARED.2018.05.011, 2018.

840 Zhou, M., Langerock, B., Wang, P., Vigouroux, C., Ni, Q., Hermans, C., Dils, B., Kumps, N., Nan, W., and De Mazière, M.: Variations and correlations of CO, C 2 H 2, C 2 H 6, H 2 CO and HCN columns derived from three years of ground-based FTIR measurements at Xianghe, China, Atmospheric Chemistry and Physics Discussions, 2022, 1–29, 2022.

Zhou, M., Langerock, B., Vigouroux, C., Smale, D., Toon, G., Polyakov, A., Hannigan, J. W., Mellqvist, J., Robinson, J., Notholt, J., et al.: Recent decreases in the growth rate of atmospheric HCFC-22 column derived from the ground-based FTIR harmonized retrievals at 16
845 NDACC sites, Geophysical Research Letters, 51, e2024GL112 470, 2024.

Zhu, Q., Wang, W., Shan, C., Xie, Y., Zeng, X., Wu, P., Liang, B., and Liu, C.: Effects of biomass burning on CO, HCN, C2H6, C2H2 and H2CO during long-term FTIR measurements in Hefei, China, Optics Express, 32, 8343–8363, 2024.